UNIVERSITY OF HELSINKI REPORT SERIES IN PHYSICS

HU-P-D148

Accelerator Mass Spectrometry and Bayesian Data Analysis

Vesa Palonen

Department of Physical Sciences
Faculty of Science
University of Helsinki
Helsinki, Finland

ACADEMIC DISSERTATION

To be presented, with the permission of the Faculty of Science of the University of Helsinki, for public criticism in the Small Auditorium (E204) of Physicum, on February 15th, 2008 at 12 o'clock noon.

HELSINKI 2008

ISBN 978-952-10-3261-5 (printed version)
ISSN 0356-0961
Helsinki 2008
Yliopistopaino

ISBN 978-952-10-3262-2 (PDF version)
http://ethesis.helsinki.fi/
Helsinki 2008
Helsingin yliopiston verkkojulkaisut

V. Palonen: **Accelerator Mass Spectrometry and Bayesian Data Analysis**, University of Helsinki, 2008, 70 p., University of Helsinki Report Series in Physics, HU-P-D148, ISSN 0356-0961, ISBN 978-952-10-3261-5 (printed version), ISBN 978-952-10-3262-2 (PDF version)

Classification (INSPEC): A0775, A2915B, A4180G, A0250
Keywords: Accelerator mass spectrometry, AMS, ion optics, instrumentation, radiocarbon, Bayesian statistics, measurement data analysis, instrumental drift, normalization to standards, continuous autoregressive process

ABSTRACT

Accelerator mass spectrometry (AMS) is an ultrasensitive technique for measuring the concentration of a single isotope. The electric and magnetic fields of an electrostatic accelerator system are used to filter out other isotopes from the ion beam. The high velocity means that molecules can be destroyed and removed from the measurement background. As a result, concentrations down to one atom in 10^{16} atoms are measurable.

This thesis describes the construction of the new AMS system in the Accelerator Laboratory of the University of Helsinki. The system is described in detail along with the relevant ion optics. System performance and some of the ^{14}C measurements done with the system are described.

In a second part of the thesis, a novel statistical model for the analysis of AMS data is presented. Bayesian methods are used in order to make the best use of the available information. In the new model, instrumental drift is modelled with a continuous first-order autoregressive process. This enables rigorous normalization to standards measured at different times. The Poisson statistical nature of a ^{14}C measurement is also taken into account properly, so that uncertainty estimates are much more stable. It is shown that, overall, the new model improves both the accuracy and the precision of AMS measurements. In particular, the results can be improved for samples with very low ^{14}C concentrations or measured only a few times.

Contents

1 INTRODUCTION

Accelerator mass spectrometry (AMS) is an ultrasensitive technique to measure the concentration of a single isotope. Historically, it was to boldly go where no other method had gone before, namely to the concentration of one atom in 10^{15} atoms (equivalent to one milligramme in a million tons of material), an accuracy of about one per cent, a sample size of the order of one milligramme, and measurement time of one hour.

Atoms from the sample are ionized (charged) in an ion source, accelerated to energies of some millions of electron volts with an electrostatic accelerator, filtered with magnetic and electrostatic fields according to their energy, momentum, and charge, and finally counted in a detector. Because high energies are used, the background from atomic or molecular ions with the same mass can be removed. This makes it possible to determine concentrations orders of magnitude smaller than conventional mass spectrometers can. Compared with decay counting, AMS can measure orders of magnitude smaller samples, important e.g. in archaeology. Measurements are much quicker since there is no need to wait for the nuclei to decay. The AMS system described in this thesis is the first and only one in Finland. At present, the accuracy of the Helsinki AMS is within 1% and the machine background is 80 kyr BP. Although the accuracy is not as as high as that of most AMS laboratories, the background of the spectrometer is among the lowest reported. The spectrometer in Helsinki is therefore especially suited for measuring old samples.

AMS measurements of unknown samples have to be normalized to measurements of known standards because the absolute throughput of an AMS machine is not known to sufficient accuracy. However, making linear interpolations between standards for normalization and taking means and standard errors of the mean of the normalized measurements is far from optimal. First, there are factors that may make the end result non-Gaussian. Hence, the 1σ interval may not contain the true value with a 68.3% probability. Second, instrumental drift and the use of the same standard measurements may introduce correlations between the measurements, which in turn will result in too small uncertainties if the correlations are not taken into account properly. Third, the standard error of the mean is a rather unstable uncertainty estimate, especially when it is known that the measurement uncertainty comes mainly from the counting statistics of the ^{14}C counts. Fourth, instrumental drift is better taken into account if it is modelled probabilistically with a continuous autoregressive (CAR) process, the parameters of which are determined from the measurements. The Bayesian model that is developed here addresses all four issues, offering better accuracy and precision for AMS results.

2 PURPOSE AND STRUCTURE OF THE STUDY

The first purpose of this study was to develop AMS capabilities for the tandem accelerator of the laboratory, document the system and assess the system's performance. Succeedingly, an emphasis was placed to develop Bayesian methods for the AMS data analysis.

The papers listed below are included in the thesis. Papers **I** and **II** deal with the AMS system and ion optics and papers **III**, **IV**, and **V** present the novel Bayesian (CAR) model for AMS data analysis. The papers are referred to in the text by their Roman numerals.

Paper I: P. Tikkanen, **V. Palonen**, H. Jungner, and J. Keinonen, *AMS facility at the University of Helsinki*, Nuclear Instruments and Methods in Physics Research B, **223-224 (2004) 35-39.**

A brief history of the use of the Helsinki tandem accelerator is presented, and changes made to the system are noted. The newly constructed AMS beam line and the first measurement to detect ^{14}C are described.

Paper II: V. Palonen, P. Tikkanen, and J. Keinonen, *Ion-optical modelling of the Helsinki AMS tandem*, Nuclear Instruments and Methods in Physics Research B, **223-224 (2004) 227-232.**

Ion trajectories are calculated for the injector, accelerator, and high-energy beam line. The injector and high-energy AMS beam line are modelled using approximative matrix calculations. The acceptance of the accelerator is obtained by calculating the electric fields numerically and ray-tracing ions through the resulting system. Some ion-optical changes to enable better matching of the injector emittance to the accelerator acceptance and of the accelerator emittance to the acceptance of the high-energy beam line are reported.

Paper III: V. Palonen, P. Tikkanen, *A shot at a Bayesian model for data analysis in AMS measurements*, Nuclear Instruments and Methods in Physics Research B, **259 (2007) 154–157.**

The first version of the new CAR model for AMS data analysis is presented. A continuous autoregressive process is introduced to describe the machine error in AMS measurements. Individual measurement uncertainties are taken to be Gaussian. Changes in the standard level are effectively integrated out by representing the posterior probability by means of a correlation matrix. First results for CAR with simulated measurement data are given, and some of the problems with the uncertainties of the conventional mean-based (MB) method are documented.

Paper IV: V. Palonen, P. Tikkanen, *An information-efficient Bayesian model for AMS data analysis*, Radiocarbon, **49(2) (2007) 369-377.**

The theory behind the CAR model is further clarified. The accuracies of the MB and CAR methods are compared as functions of increasing trend strength. CAR is shown to be more accurate overall. Also the reliabilities of the uncertainties given by the methods are compared. While uncertainties given by CAR are reliable, MB uncertainties may have only a 50% chance of containing a true value.

Paper V: V. Palonen, P. Tikkanen, *Pushing the limits of AMS radiocarbon dating with improved Bayesian data analysis*, Radiocarbon, **49(3) (2007) 1261-1272.**

> The theory behind the CAR model is further improved by describing the trend with hidden variables and the measurement errors with Poisson distributions. This approach improves the results for very old samples. First results on the stability of the CAR uncertainty estimates are given.

The Helsinki AMS system is the result of a group effort. In particular, Dr. P. Tikkanen, Mr. K. Wahlström, Mr P. Siiki, and I contributed to get the machine in operation. My main contributions were to carry out the measurements and data analysis, design some of the new components and ion optical improvements for the system, improve the accelerator control and measurement data acquisition, and maintain the ion source. I made a fair contribution to paper **I**, initiated and developed the models detailed in papers **II** to **V**, coded and applied the necessary inferential algorithms, did the simulations, and wrote papers **II** -**V**.

The following chapter, chapter 3, covers the principles of AMS. Chapter 4 describes the AMS setup in the Accelerator Laboratory and gives an overview of the modifications that were carried out. The ion optics of the accelerator system are also reviewed in this chapter. Chapter 5 describes some of the radiocarbon measurements that were done. The novel CAR model for the analysis of AMS measurement data is developed in chapter 6. Improved precision and other advantages of the model are demonstrated in chapter 7. Finally, chapter 8 presents the conclusions for the present work and suggests directions for future research.

3 INTRODUCTION TO AMS

The principle of accelerator mass spectrometry (AMS) is simple, namely, to separate one isotope from a huge amount of atoms and molecules. The separation is achieved with an electrostatic accelerator, several electrostatic and magnetic analysers, and collisions with other atoms. Advantage is also taken of the fact that not all atoms form negative ions.

Figure 1 illustrates the difference between conventional mass spectrometry (MS) and AMS. In conventional MS, background reduction in a spectrum is limited by the presence of molecules and atoms of almost the same mass and by tails of the peaks of nearby abundant atoms. In the measurements of ^{14}C , the background from interfering ions limits the MS abundance sensitivity to 10^{-11} - 10^{-6} [1]. The AMS setup includes an accelerator and additional analysers. The high energy that is used enables the destruction of interfering molecules and identification of the atomic number of the ions. Concentrations lower than one atom in 10^{15} atoms can be measured.

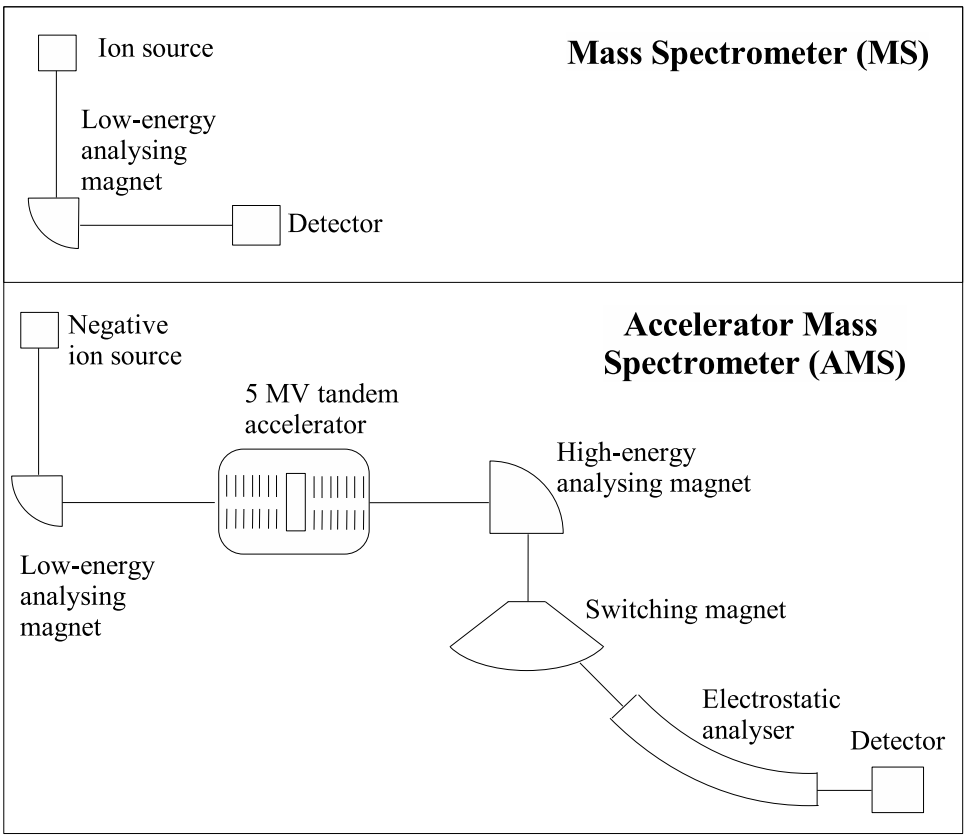

Figure 1: A schematic comparison of conventional MS and AMS.

The first AMS measurement was done in 1939 when ^{3}He was detected with the 88-inch Berkeley cyclotron [2]. The first proposal for ^{14}C measurements was made in 1977 [3]. In the same year, two groups working independently at McMaster University and the University of Rochester made

the first direct measurements of ^{14}C with electrostatic accelerators [4, 5]. AMS methods for the detection of other isotopes were quickly realized: for ^{10}Be in 1978 [6] and then for ^{26}Al [7], ^{36}Cl [8], ^{41}Ca [9], and ^{129}I [10]. At present, over 30 different isotopes have been measured. AMS has become a powerful and widely used technique with applications in many branches of science. Radiocarbon measurements are of interest in archaeology, geology, cultural heritage, biological sciences, radiation protection, aerosol science, and environmental studies. There is a growing interest in cosmogenic isotopes such as ^{10}Be and ^{36}Cl. Multiple review articles and conference proceedings describe the many applications [11–26]. Worldwide, more than 50 laboratories have developed or bought AMS capabilities. Experimental parameters for most of the isotopes measured by AMS are listed in table 1.

At present, the trend in instrumentation is to move to smaller accelerators. A long-standing and wrong assumption was that a charge state of 3+ or higher was needed to get rid of the interfering molecules. With this assumption relaxed, it has been possible to develop smaller AMS machines with accelerating voltages as low as 200 kV. Smaller machines reach sufficient precision and are cheaper and easier to operate, but the background is larger than in bigger machines and the measurable isotopes are fewer.

Regardless of the type of AMS system, there are three basic requirements for a successful AMS measurement:

- Sufficient reduction of the amount of unwanted atoms. The abundance of a rare isotope may be as low as one part in 10^{15}. Events that are normally rare may easily become dominant relative to the small amount of the rare atoms. For example, collisions of the abundant unwanted ions with residual-gas atoms in the vacuum or the beam line components cause charge exchanges and scattering to different angles, making it possible for the ions to pass analysers that they otherwise could not pass.

- Constant throughput of rare isotope counts and the abundant isotope current. As a measurement system, the AMS setup is complex. The electric and magnetic fields fluctuate and samples give different currents. Rare and abundant isotopes are measured in different places of the beam line. For accurate estimates of the concentration, the ratio of the throughputs of the isotopes should stay constant between the measurement of unknown samples and the measurement of standard samples.

- Sufficient current. Since the target isotopes are usually very rare, the original amount of ions taken from the sample should be large and the throughput of the accelerator system high in order to gather enough rare atoms to obtain sufficient precision for the result.

This thesis concerns the measurement of the isotope ^{14}C , the isotope with most applications both in volume and in number. ^{14}C is also the most demanding isotope, with some of the applications

requiring almost an order of magnitude better precision than most applications of the other isotopes. Because of the high terminal voltage, the Helsinki AMS is extendible to the measurement of several other isotopes, for example, ^{7}Be, ^{27}Al, and ^{36}Cl.

Table 1: Experimental AMS parameters. Reprinted from [1].

Sample	Ions	I [μA]	V [MV]	q [e]	E_{tot} [MeV]	Detector	Detection limit	Ref.
^{2}H, ^{3}H								
^{2}H g	H+		1.5	1+	1.5	f + Si	10^{-14} T/D	[27]
^{3}H g	H+		Cycl	1+	22	f + Si	4×10^{-14}	[28]
^{3}He								
He g	He-	0.02	0.8	2+	2.4	f + Si	$< 10^{-10}$	[29]
^{7}Be								
BeO	BeO-		2.2	2+/4+	6.6	f + g, dE, E_r	$< 10^{-15}$	[30]
^{10}Be								
BeO	BeO-	1	2	2/3+	4.8	f + g, dE, E_r	3×10^{-15}	[31]
BeO	BeO-	10	6	3+	20.3	f + g, dE, E	6×10^{-15}	[32]
^{14}C								
Graphite	C-	40	4.5	1+-4+	18	g, dE, E	5×10^{-16}	[33]
^{22,24}Na								
Na_2CO_3+Fe	Na-	0.02	5	7+	40	g, dE / SiE	1×10^{-11}	[34]
^{26}Al								
Al_2O_3+C	Al-	0.2	1.9	3+	7.6	g, dE, E	5×10^{-15}	[31]
Al_2O_3	Al-	3	7.5	7+	60	g, dE, E	3×10^{-15}	[35]
^{32}Si								
SiO_2	Si-	0.10	9.2	5+g	55.2	g, dE, E	$> 6\times10^{-14}$	[36]
K_2SiF_6	Si-	0.001	8	9+	80	f + Mag + g, dE, E		[37]
^{36}Cl								
AgCl	Cl-	15	12	10+	132	g, dE, E	1×10^{-15}	[38]
AgCl	Cl-	5	8	7+	64	g, dE, E	5×10^{-15}	[39]
^{41}Ca								
CaH_2	CaH^{3-}	5	8.5	8+	76	g, dE, E	6×10^{-16}	[40]
^{53}Mn								
Mn, CrOx+Ag	MnO-		Tan + Lin	25+	292	Bragg	1.0×10^{-10}	[41]
^{55}Fe								
Fe	Fe-		11	10+	132	TOF + Bragg	8×10^{-13}	[42]
^{59}Ni								

Ni	Ni-	0.5	14.5	13+	203	f + Mag + g, dE, E	5×10^{-13}	[43]
^{60}Fe								
Fe	Fe-	0.006	Tan + Lin	9,18, 20+	320	f + Mag + g, dE, E	$>10^{-12}$	[44]
^{63}Ni								
Ni	Ni-					GFM + g, dE, E	10^{-14}	[45]
^{79}Se (CdSe)					100			[46]
^{90}Sr								
SrH_2	SrH_3^-		11	11+			2×10^{-13}	[47]
^{107}Pd								
Pd						GFM + TOF + g, dE	10^{-8}	[48]
^{129}I								
AgI	I-		0.75	5+	4.5	Si, E	5×10^{-13}	[49]
AgI	I-	5	5	5+	30	TOF	5×10^{-14}	[16]
AgI+Ag	I-		11.8	11+	140	TOF, Si, E	3×10^{-13}	[50]
^{126}Sn								
Sn	Sn-		5	5+	30	g, E, f + X	9×10^{-6}	[51]
^{138}Ba								
Ba	Ba-		1.75	5+	10.5	Si, E		[52]
^{205}Pb								
Pb	Pb+	Low	Lin	9/29+	2300	Mag + TOF + g, dE, E	1.0×10^{-12}	[53]
U,Pu,Np								
^{236}U+Nb	UO^-	0.6 nA	1.60	5+	9.5	g, E	5×10^{-8}	[54]
^{237}Np, Feox			5	7+	40	g, E	10^5 at	[55]
^{239}Pu, Feox	Pu^-		3.5	7+	28	g, E	5×10^5 at	[55]
^{240}Pu, Feox							1.3×10^6 at	[55]
^{242}Pu, Feox							2.7×10^6 at	[55]
^{244}Pu, Feox							7.1×10^6 at	[55]

E_{tot} = final energy (MeV). Detector types: f = foil, g = gas, X = X-ray detection, dE = energy loss measurement, E = total energy measurement, E_r = residual energy, Si = silicon detector, Mag = magnet, TOF = time-of-flight measurement, GFM = gas-filled magnet.

4 HELSINKI AMS

This chapter intoduces the Helsinki AMS setup and gives a short overview of the modifications made to the original accelerator system. After the system description, the calculated ion paths in the injector, the accelerator, and the AMS beam line are given. Finally, the AMS measurements and the mean-based method of data analysis, which is used as a fast check during the measurements, are described.

4.1 Present AMS system

The schematic layout of the present AMS system is shown in Figure 2. Asterisks indicate new or modified parts of the system.

The first part of the system is the 40-sample ion source (MC-SNICS, manufactured by the National Electrostatics Corporation). A photograph and a schematic drawing of the principle of operation of the ion source are presented in Figure 3. The current of the $^{12}C^{-}$ beam from this source is typically 10-20 μA. Note: all currents are given here as electric currents (as distinct from particle currents).

The ion source is followed by an einzel lens and a preaccelerating column. The electrostatic analyser (radius of curvature 0.5 m, effective bending angle 40°, electrode separation 53 mm) removes particles from the low-energy tail of the ion beam. The two-sided 90-degree injection magnet (radius of curvature 0.3 m, ME/q^2 value of 13.3 u MeV/e^2) is the first momentum-analyser in the system. It selects the desired mass into the accelerator. The cycling of isotopes entering the accelerator is achieved by changing the field of the injector magnet. After the injector magnet, an electrostatic triplet, $x-y$ steerer, and x-deflector are used to fit the beam focus, offset, and angle to the accelerator acceptance.

The accelerator is a vertical belt-driven 5-MV tandem of the Russian EGP-10 type [56, 57]. The accelerator is equipped with inclined-field accelerating tubes. Each of the four tubes is 2200 mm long. The first tube includes an immersion lens and a section of straight electrodes at the entrance. After two accelerating tubes there is a 545-mm-long, 8-mm-diameter stripper canal, with CO_2 or Ar gas used for charge exchange of the ions. The entrance angle of the ion beam to the high-energy accelerating tubes can be adjusted with the terminal steerer to correct for the effects of the inclined fields of the tubes.

Figure 4 shows the charge state fractions as a function of the incoming ^{12}C ion energy in argon gas [58]. Similar charge state fractions are expected for CO_2 gas. As can be seen, the maximum yield for the 3^{+} charge state of ^{12}C is obtained at an energy of approximately 2.6 MeV. Because charge exchange with the stripper gas is mainly a velocity-dependent phenomenon, the maximum yield for ^{14}C is expected to be at about 3.0 MeV.

The terminal voltage of the accelerator is stabilized by using either the generating voltmeter (GVM)

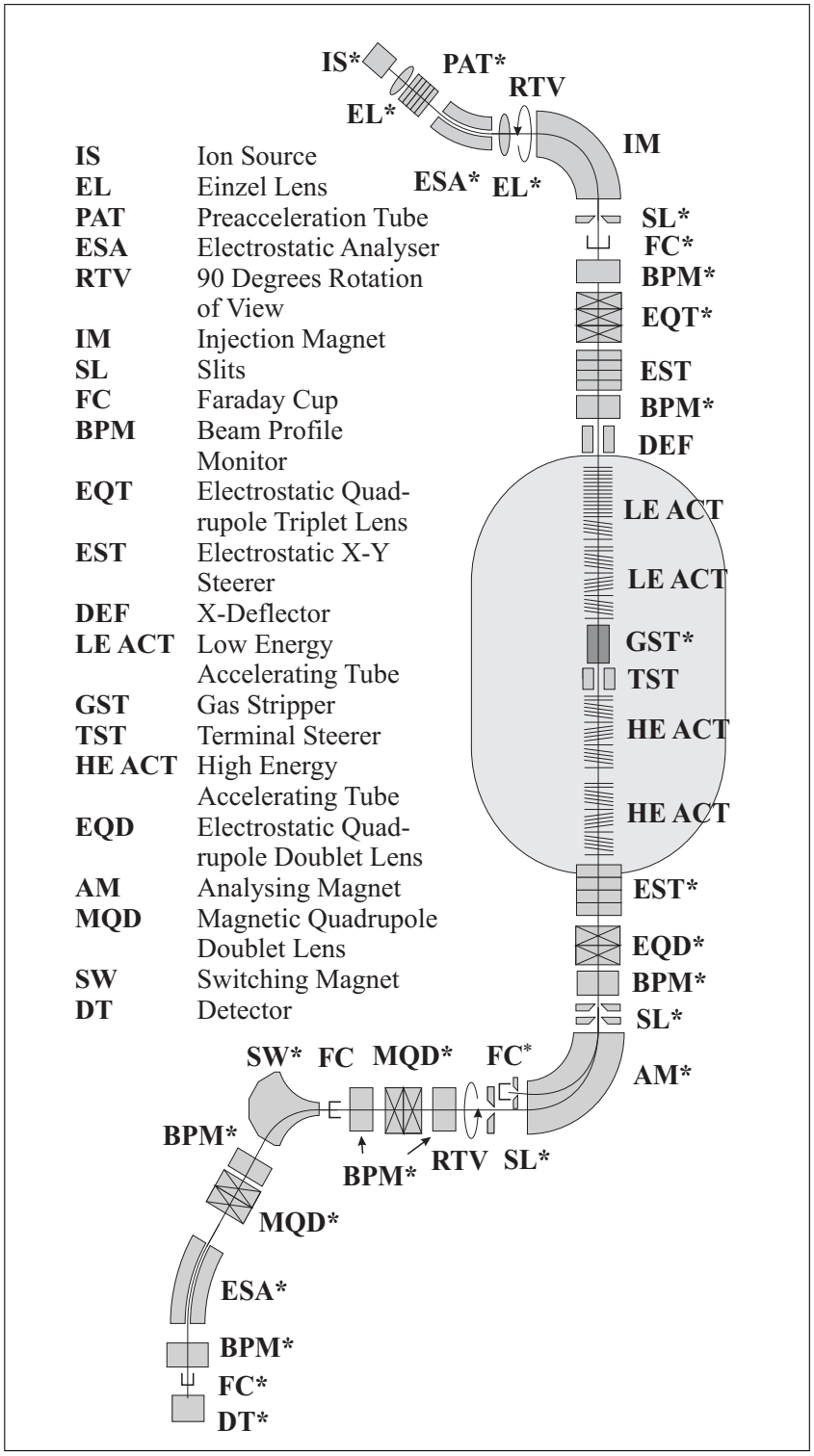

Figure 2: Schematics diagram of the tandem accelerator. Components relevant to AMS are shown. Asterisks indicate new or modified parts which were installed to upgrade the accelerator system for AMS use. Adopted from paper **I**.

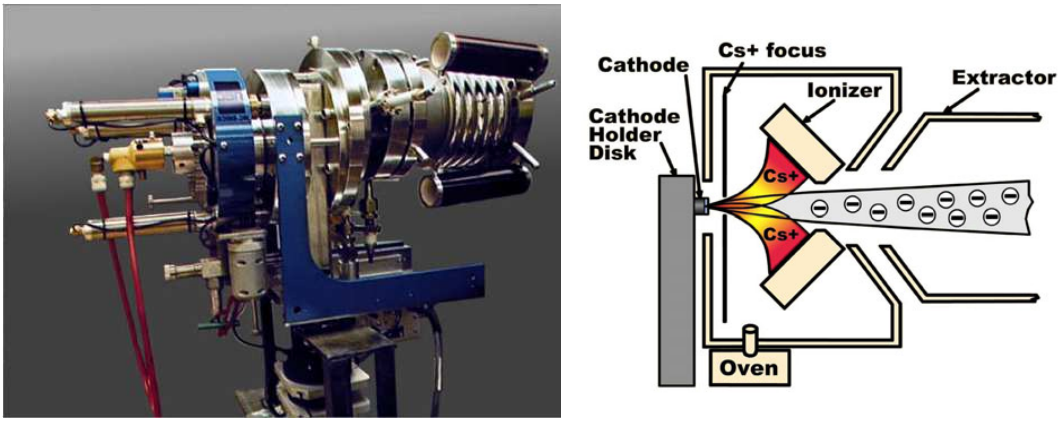

Figure 3: Photograph of the MC-SNICS ion source and a schematic drawing of the principle of operation (courtesy of National Electrostatics Corporation). Positive caesium ions are accelerated onto the sample. The caesium ions sputter carbon atoms out of the sample. Some of the sputtered carbon atoms have negative charge and can be (pre)accelerated and injected into the tandem accelerator.

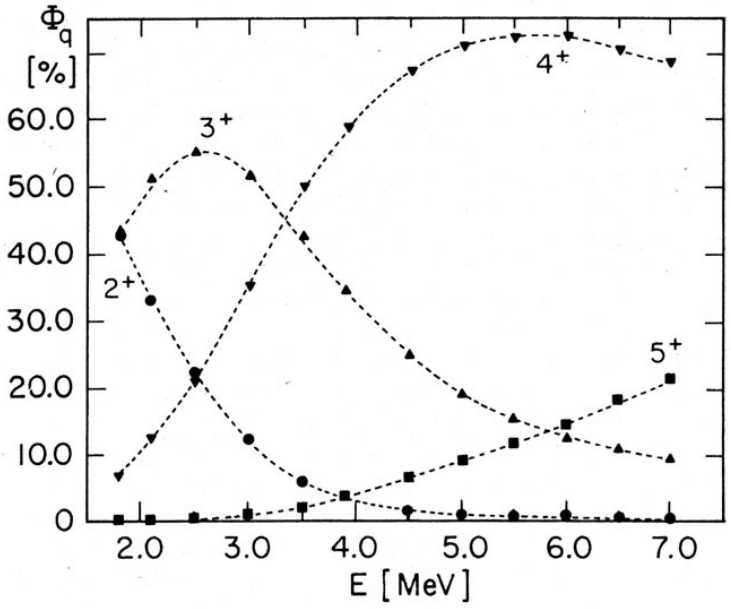

Figure 4: Charge state fractions of ^{12}C ions as functions of the incoming ion energy after an argon gas target of about $\sim 3\mu g/cm^2$ thickness. From [58].

and the capacitive pick-up ring (CPU) or the CPU and the off-axis slits at the focus plane of the analysing magnet. At present, the GVM+CPU stabilization option results in too high voltage fluctuations for AMS use and therefore the terminal voltage is stabilized with the CPU and the off-axis slits. During ^{13}C measurements, the voltage stabilization is accomplished with a 100-500

nA $^{13}C^{3+}$ current, and during ^{14}C measurements with a roughly 0.1-10 nA $^{13}C^{3+}$ current from $^{13}CH^{-}$ molecules. The currents change from sample to sample, and in order to keep the throughput constant, the magnitude of the slit stabilization signal has to be made independent of the current. Additional electronics prior to the main stabilization electronics divide the currents from the slits by their sum. After numerous modifications to the charging system, the terminal voltage at 3 MV (12-MeV carbon ions) is stable to better than ± 2 kV (peak to peak), with the root mean square ripple being less than 0.7 kV.

The first component in the high-energy beam line is the $x-y$ steerer, which corrects the possible beam offset caused mainly by the inclined field of the accelerator. The ions are focused with an electrostatic quadrupole doublet to the object plane of the analysing magnet, where movable slits in both x and y directions are used to define the object size, which in turn affects the resolution of the magnet. The analysing magnet (90-degree, radius of curvature 1.5 m, ME/q^2=240 u MeV/e^2, single-focusing with perpendicular Rogowski-shaped entrance and exit poles) is used as the main momentum selector. The off-axis chamber following the magnet houses an off-axis Faraday cup with slits for the simultaneous terminal voltage stabilization and measurement of the stable isotope current. Another set of off-axis slits is included for beam energy stabilization during the measurements of a rare isotope.

A magnetic quadrupole doublet lens and a switching magnet follow the analysing magnet. The switching magnet is used for further momentum analysis and selects the AMS beam line at -60° (radius of curvature 1.2 m, ME/q^2=77 u MeV/e^2). The main components of the AMS beam line are a magnetic quadrupole doublet, electrostatic analyser, and detector. The 30-degree cylindrical electrostatic analyser (radius of curvature 2.00 m, E/q=7.2 MeV/e) acts as a high-resolution energy analyser. Ions of a rare isotope are finally counted in an ion-implanted silicon detector with an active area of 100 mm^2 located at the end of the beam line. A Faraday cup can be moved in front of the detector during beam optimization with an abundant-isotope pilot beam.

4.2 Modifications done for AMS

The present AMS system is the result of significant modifications to the original accelerator system. Starting with the injector, none of the previously existing ion sources could be used for AMS and a new ion source had to be purchased and installed. The tandem accelerator had originally been designed for protons and it was necessary therefore to calculate the ion optics of the whole system for heavier ions than protons. The beam line for AMS was then designed on the basis of the ion-optics calculations. Improvements were also made to the injector, accelerator terminal, and high-energy beam line. In addition, several changes were made to the charging system of the accelerator to improve the stability of the terminal voltage. New NEC stabilization electronics replaced the old stabilization system, which had no CPU stabilization capability. The charging belt was changed several times, and several methods for charging the belt were tested. Several

improvements were made to the vacuum system, among these the installation of a turbo molecular pump to the accelerator terminal.

The sequential measurement of the abundant and rare isotopes in an AMS measurement meant that the vacuum chamber of the analysing magnet and the subsequent part of the beam line had to be redesigned to facilitate both measurement of the current of an off-axis ion beam and stabilization of the terminal voltage with the same beam. The continual changes of isotopes and samples also meant that most parameters of the system had to be computer controlled. The automation of the acceleration system was carried out in parallel with the other modifications. Because AMS requires a much higher quality of the ion beam, beam diagnostics were improved significantly by installing seven beam profilometers along the AMS system. A list of the accelerator modifications can be found in Appendix A.

4.3 Ion optics

4.3.1 Basic definitions

The following three sections deal with ion paths in the spatial (x,y)-coordinates perpendicular to the central reference path of the ion beam (optical axis) and with tilt angles of ion momenta with respect to the reference path, $a = p_x/p_z$, $b = p_y/p_z$. The perpendicular coordinates are treated as functions of the reference path length z. Figure 5(a) illustrates the choice of coordinates.

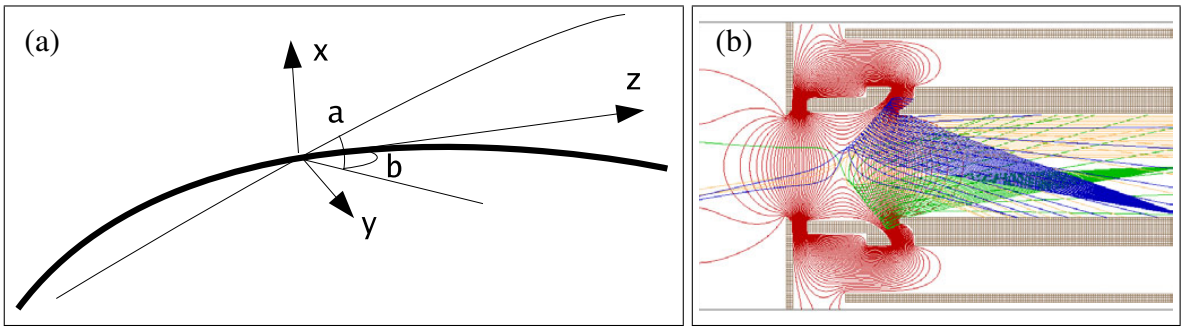

Figure 5: (a) Choice of coordinates for ion optics calculations. (b) The equipotential lines (red) and ray-traced secondary electron paths (blue, green, yellow) of an optimized Faraday cup at the end of the AMS beam line.

To calculate the paths of ions, one has to calculate the magnetic and electric fields affecting the ions. Since analytic solutions to the Maxwell equations are possible only for simple geometries, numerical algorithms are used. Fields are calculated numerically by dividing the geometry into small elements and then solving the appropriate differential equation for the mesh. The finite difference method was used in this work. Once the field has been calculated, it is straightforward

to fly ions through the components. As an example, Figure 5(b) shows the equipotential lines and ray-traced secondary electron paths of an optimized Faraday cup at the end of the AMS beam line.

Electrostatic and magnetic analysers can be approximated with simple uniform fields. These approximations are mostly used to obtain simple analytic expressions for ion paths to ascertain which ions will get through the analyser and to scale the field for different ions. Hence, in a uniform magnetic field B, an ion with mass M, charge q, and kinetic energy E has a circular path with a radius of curvature r [1]

$$2\frac{ME}{q^2} = (Br)^2. \tag{1}$$

Correspondingly, in a radial electrostatic field $\mathscr{E}$

$$2\frac{E}{q} = \mathscr{E}r. \tag{2}$$

Projections of the ion beam in the (x,a) and (y,b) planes can be represented with two 2×2 matrices σ_x, σ_y defining two ellipses:

$$\begin{pmatrix} x & a \end{pmatrix} \sigma_x^{-1} \begin{pmatrix} x \\ a \end{pmatrix} = 1, \quad \begin{pmatrix} y & b \end{pmatrix} \sigma_y^{-1} \begin{pmatrix} y \\ b \end{pmatrix} = 1. \tag{3}$$

The 2D emittances are then given as the area of the ellipses. The beam line components can now be conveniently described with transfer matrices R (to first order), relating the beam ellipse before a component to the ellipse after it:

$$\sigma_{\text{after}} = R\ \sigma_{\text{before}} R^{\text{T}}. \tag{4}$$

4.3.2 Injector

Figure 6 shows the first-order matrix calculation for the injector done with GRAPHIC TRANSPORT code [59] (see Figure 2 for the abbreviations). Before the 20 kV preaccelerating column, the MC-SNICS ion source has an emittance of about 4.2 π mm mrad MeV$^{1/2}$ with a 1 mm half-size and 30 mrad half-angle at 20 keV energy [60]. With the present equipment, the best throughput is obtained when the beam is focused to the centre of the cylindrical electrostatic analyser. An einzel lens immediately after the analyser is used to reduce the size of the beam in the injection magnet. As a result of the calculations, to improve beam throughput, the original iris diaphragm with maximum aperture of 25 mm (the component SL in Figure 6) was replaced with adjustable slits with a 45 mm maximum aperture. An einzel lens after the slits was also replaced with an electrostatic quadrupole triplet. The triplet enables independent focusing in both directions, and the 70 mm aperture enables larger angular spread of the beam to the accelerator. This improves the matching between the injector emittance and the acceptance of the accelerator.

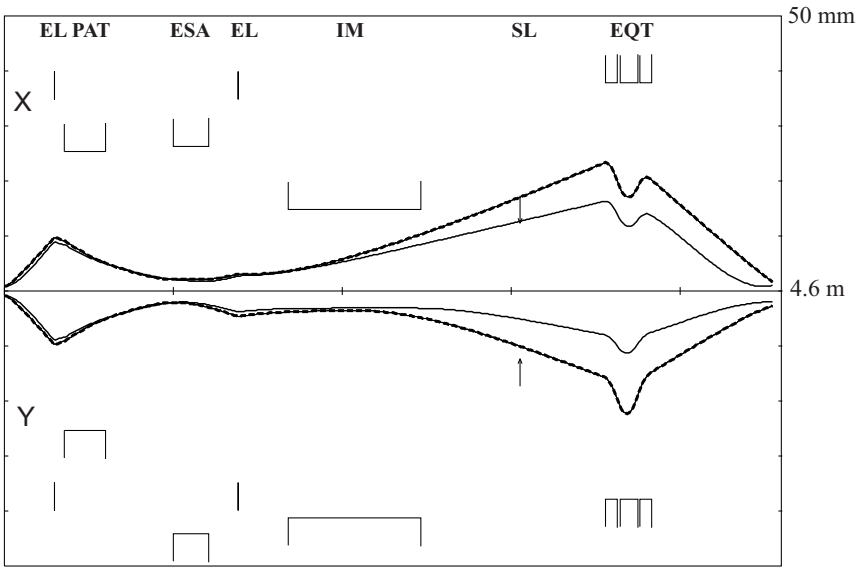

Figure 6: Beam envelopes for 40-keV $^{12}C^{-}$ ion beam in the injector of the Helsinki AMS system. The dashed envelopes represent a calculation where the effect of the linear space charge of a 100-μA beam current and a momentum deviation of $\Delta p/p$ of 1% are included. Such effects were neglected in the calculation of the solid envelopes. Adopted from paper **II**. The abbreviations are explained in Figure 2.

4.3.3 Accelerator

In the direction of the effect of the inclined field of the accelerator (x), optimal incoming beam position and inclination differ for each ratio of injection energy to the terminal voltage (see paper **II**). Beam position and tilt are controlled with an $x-y$ steerer and x deflector before the accelerator. Electric fields of the low-energy accelerating tubes and immersion lens were calculated with the Simion 7.0 code [61]. Figure 7 shows the electrostatic potential of the first 1.2 m of the accelerator including the deflector and the immersion lens.

In order to obtain the acceptance of the accelerator, in total 20 000 ions were ray-traced through the accelerator from the z position of the beam profile monitor close to the accelerator entrance and from random (x,a,y,b) positions. Acceptance of the accelerator is then defined by the area of the starting coordinates of those ions that made it to the 10-mm-diameter stripper canal. These ions are represented with dots in Figure 8, which shows the case of 40 keV injection energy and 3 MV terminal voltage. The corresponding phase-space ellipses are calculated from the ion coordinates with the following equations [62]:

$$\begin{aligned} \sigma_{11} &= 4\left\langle x^2 \right\rangle, \\ \sigma_{12} &= 4\left\langle xa \right\rangle, \\ \sigma_{22} &= 4\left\langle a^2 \right\rangle, \end{aligned} \tag{5}$$

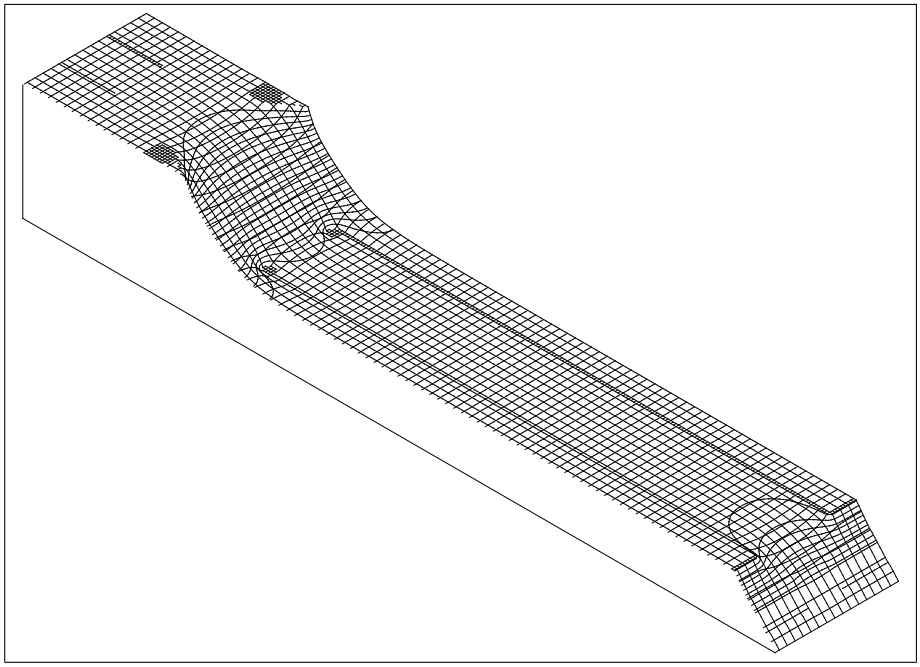

Figure 7: Distribution of the electrostatic potential (as experienced by negative ions) in the first 1.2 metres of the first low-energy accelerating tube, including the immersion lens and x-deflector. Height of the surface represents the potential. Equipotential lines have a spacing of one-thousandth of the terminal voltage, the total height in the figure representing about 5% of the terminal voltage.

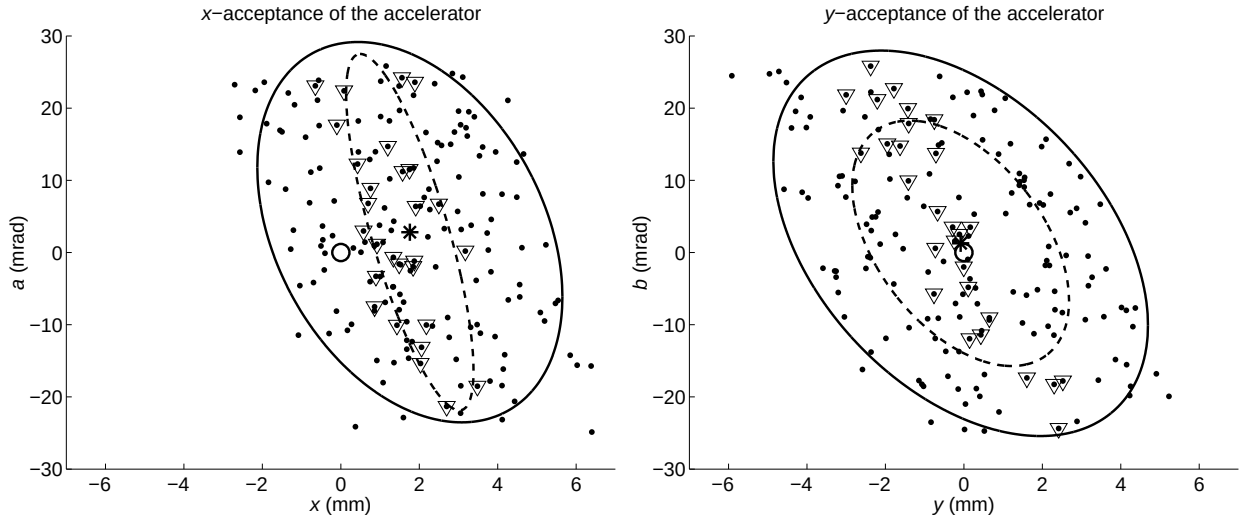

Figure 8: Matching of injector emittance to accelerator acceptance for the case where $E_{\mathrm{inj}} = 40$ keV and $U_{\mathrm{term}} = 3$ MV. Dots and solid ellipses represent the acceptance with a 10-mm-diam stripper canal. Dashed emittance ellipses represent the injector emittance with space charge and momentum dispersion included. The optical centre of the beam tube is denoted with a small open circle ($\circ$) while the centre of the acceptance ellipse is marked with a star (*). Triangles (∇) represent the acceptance of the original 4-mm-diam. stripper canal. From paper **II**.

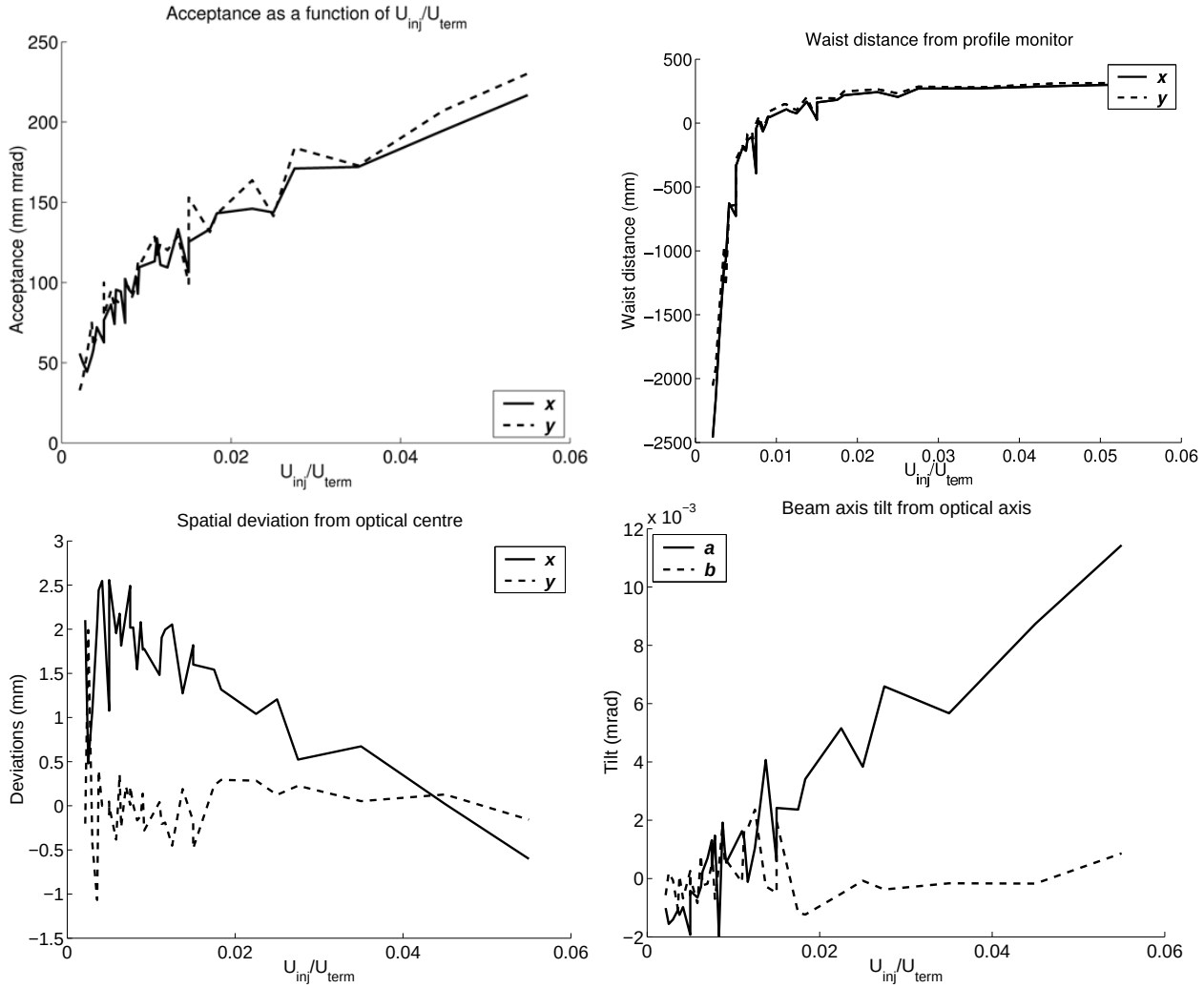

Figure 9: Upper left: Acceptances in both directions as a function of $U_{\mathrm{inj}}/U_{\mathrm{term}}$. Upper right: Waist positions relative to the beam profile monitor position near the accelerator entrance. Lower left: acceptance offset relative to optical center. Lower right: acceptance tilt relative to optical axis.

Table 2: Beam emittances in different parts of the system. All values in π mm mrad.

	Emittance	
Location	x	y
Before stripper	13.1	11.1
After stripper	16.5	14.3
After accelerator	8.27	7.37

where $\langle . \rangle$ denotes an average over the simulated ions. The phase-space ellipses are denoted by the solid ellipses in Figure 8. Dashed emittance ellipses represent injector emittance with space charge and momentum deviation included (see section 4.3.2). The small circle indicates the optical centre of the beam line, and the star indicates the centre of the acceptance. The difference between the centre of the acceptance and the optical centre is due to the inclined field structure. Triangles represent ions that would have passed a 4-mm-diameter stripper. They therefore define the acceptance of the old setup.

Acceptances were computed for 35 different $U_{\mathrm{inj}}/U_{\mathrm{term}}$ values. Figure 9 shows the acceptances shown as a function of $U_{\mathrm{inj}}/U_{\mathrm{term}}$ along with waist positions (the point of minimum beam size) and offset and tilt angle from the optical centre. Waist positions are relative to the beam profile monitor position near the accelerator entrance. (Figure 9 is a corrected version of the figure in paper **II**.)

Calculated acceptances show that it is possible to achieve a 100% transmission of the injected beam to the accelerator. It is also possible to use the results in Figure 9 for faster beam optimization.

Increase of the beam emittance in the stripper increases with beam spot size in the stripper [63, 64]. Since it is difficult to estimate the size of the beam in the stripper during real measurements, the maximum emittance of the beam from the stripper was calculated and used in the subsequent calculations for the high-energy AMS beam line. The maximum emittance for AMS was obtained by ray-tracing the whole accelerator acceptance with the added emittance increase in the stripper through the high-energy accelerating tubes. The growth in 2D emittance due to the stripper gas was about 30% (paper **II**). The calculation was done assuming a 40 keV injection energy and a 3 MV terminal voltage with typical AMS runs in view.

To model the lens effect of the high-energy inclined fields properly, three points from the perimeter of the ellipse were ray-traced through the high-energy side of the accelerator and their coordinates after the accelerator were used to calculate the sigma matrix of the beam after the accelerator. The sigma matrices in both projections were then used in the study of the high-energy beam line. Table 2 gives the calculated emittances before and after the stripper, and after the accelerator.

As already noted, the inclined-field accelerating tubes were originally developed for the acceleration of protons. In order to compensate for the effect of the inclined field and obtain better

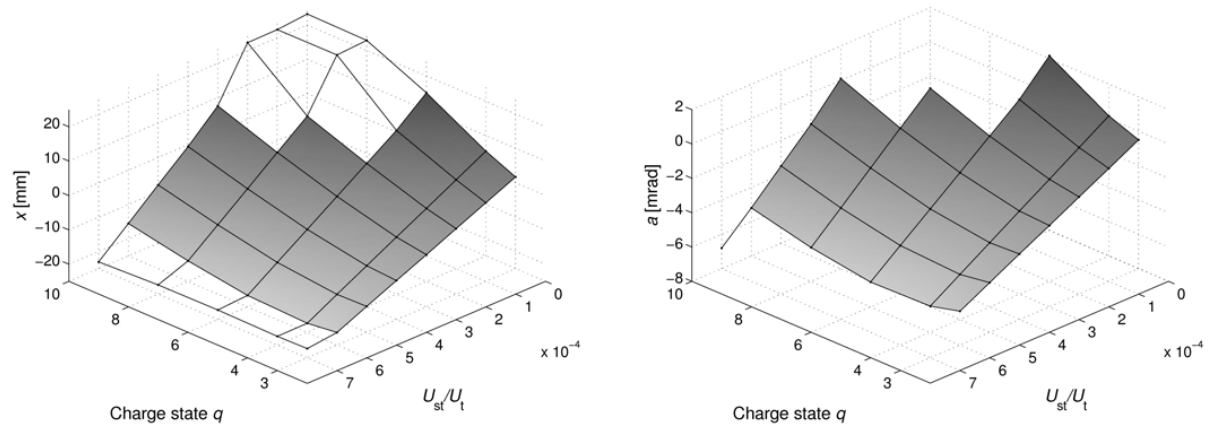

Figure 10: Spatial and angular offsets after the accelerator due to the terminal steerer shown for different charge states. U_{st} denotes the steerer voltage, U_t the terminal voltage. At roughly ± 20 mm, the beam hits the walls of the accelerating tube.

throughput for higher charge states [64], an electrostatic deflector, or terminal steerer, was installed into the terminal after the stripper. Different steerer voltages are needed for different charge states, and the effect of the steering has to be corrected with the $x-y$ steerer positioned after the accelerator. Figure 10 shows the offsets of the beam from the optical axis at the end of the accelerator for different steerer voltages and charge states. It can be seen that, for the charge state $3+$ used for AMS, the steerer should not be used at all. Indeed, best ^{14}C throughput is obtained with the steerer at zero volts. However, for the high charge states a small negative tilt after the accelerator is unavoidable when optimizing the throughput.

4.3.4 High-energy beam line

In Figure 11, the above-estimated maximum emittance of the accelerator is taken through the high-energy beam line. The calculation was done to the second order using the COSY INFINITY [65–67] code. Additional rays in both directions represent ions with a 10 keV energy deviation from the 12.04 MeV central path. Since the off-energy rays reach the detector within the spot size and do not suffer too large deviations along the beam line, the effect of the terminal voltage ripple in the measurements should be small. As can be seen, the maximum emittance is at the limit of what the AMS beam line can deliver to the detector. In addition to the design of the AMS beam line on the basis of the ion optics calculations, a 10° iron clamp was installed at the exit of the switching magnet to reduce the exit angle to 10°. The clamp reduces the magnet's focusing of the ion beam in the vertical direction and increases focusing in the horizontal direction, enabling the use of smaller vertical beam in the switching magnet and better focusing for the rest of the beam line. The clamp also moves the point of exit a bit closer to the optical axis, correcting for the poor design of the

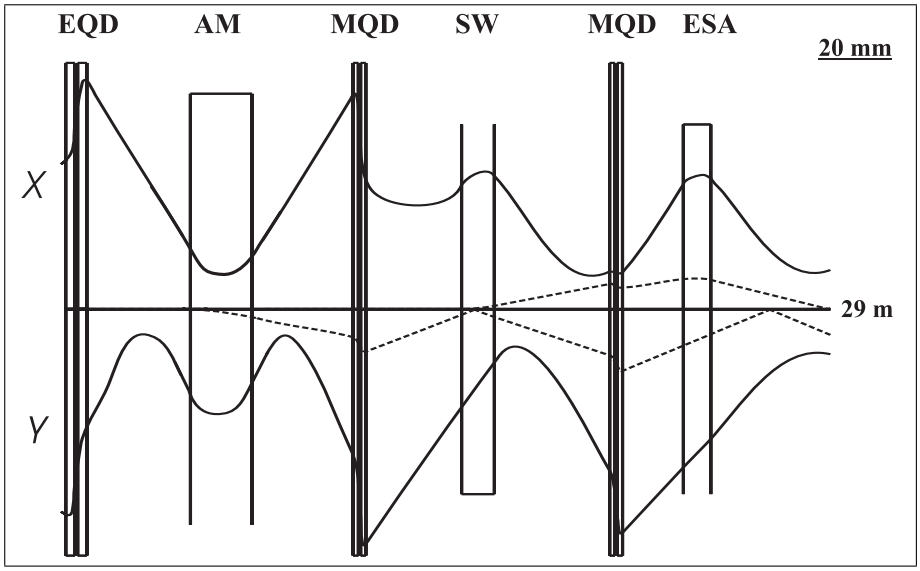

Figure 11: Beam envelope of the high energy beam line calculated with the maximum emittance. Dashed lines are ions with 10 keV energy deviation. The vertical scale represents a 20-mm half-width in both directions. The total length of the beam line is 29 metres. From paper **II**. The abbreviations are explained in Figure 2.

magnet. Beam tests were done with and without the clamp and, in accord with the calculations, the new arrangement gives a better throughput.

The real 2D emittance is estimated to be almost half of the maximum 2D emittance used in this calculation. This is because calculations for the emittance used the acceptance of the accelerator instead of the emittance of the injector, and also the largest estimate of the angular straggling in the stripper was used. It is concluded from the ion-optics calculations that a 100% transmission can be obtained for the high-energy AMS beam line. Indeed, the measured ion-optical throughput of the whole system seems to be over 95% (see section 5.2).

4.4 Measurements

4.4.1 Accelerator control

All essential parameters of the accelerator are computer-controlled. The total number of inputs and outputs in the accelerator control system is roughly 400. Presently most of the control tasks are distributed to local intelligent control units, called CAN boxes, which are located near the instruments. Work is underway to change the automation system of the laboratory from the home-made CAN components to commercial components from Allen-Bradley. The main advantages of the commercial system are reliability, the easy availability of new and spare parts, and centralized and easy programming of all the I/O points in the field. The graphical operator interface is built on

a normal PC computer running on a Windows-XP operating system.

The CAN-based control system of the accelerator is flexible enough to be used also for the acquisition of rare isotope counts. A dedicated CAN box with the faster DeviceNet protocol has been constructed for this purpose. The pulse-height information from the main amplifier is digitized in a 100-MHz Wilkinson ADC, which is controlled and read by the dedicated CAN box.

A database (IndustrialSQL) has also been connected to the automation system. The ^{14}C isotope rate, the ^{13}C current, and selected accelerator parameters from the CAN or Allen-Bradley networks are stored in the database. Hence, parameters like the injector magnet field, ion source parameters, terminal voltage, and quality of the vacuum are stored in realtime. Quality control is improved as a result, with the possibility to make queries to the database during, and, when necessary, after the measurements.

4.4.2 Measurement cycle

Figure 12 illustrates the AMS measurement cycle. The sample wheel is rotated several times. Usually samples are measured in the order they sit in the sample wheel. During each cycle, four ^{13}C measurements and three ^{14}C measurements, lasting about ten minutes in total, are made for each sample. Total time for a measurement run is over 30 hours.

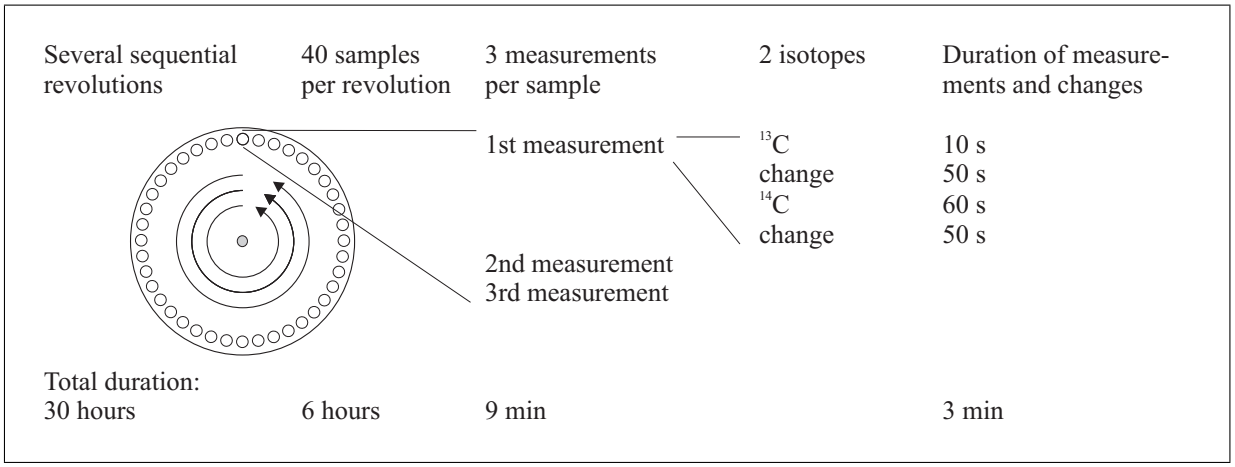

Figure 12: Typical measurement cycle for AMS measurement of ^{14}C .

The 40-sample wheel contains about 25 unknown samples, 10 standards, an aluminium sample, and a couple of almost ^{14}C -free samples (blanks), some of which have gone through normal sample preparation.

4.4.3 Mean-based method of data analysis

In this section, a mean-based (MB) method for data analysis similar to that of Elmore et al. [68] is described. Although not optimal, this method is fast and adequate for use during the measurements. A more rigorous method (the CAR model) for calculating the standard level and normalizing the unknown samples to the standard level is presented in section 6.3.

As shown in the previous section, the measurement of a sample consists of one or several ^{13}C and ^{14}C measurements, each of which gives a ratio $R_i = (^{14}\mathrm{C}/^{13}\mathrm{C})_i$. However, because absolute throughput and isotopic fractionation in the AMS system are not known to sufficient accuracy, standard samples with known ^{14}C concentrations have to be measured periodically to convert the measured $^{14}\mathrm{C}/^{13}\mathrm{C}$ ratios to concentrations. Some fractionation of the isotopes may also have occurred in nature before the measurements and will be corrected for by using the δ^{13}C values of the samples measured with a separate mass spectrometer. A δ^{13}C value is simply the difference, in per mils, between the $^{13}\mathrm{C}/^{12}\mathrm{C}$ ratio of the sample and that of a PDB standard.

The standard level at the temporal point of a measurement of an unknown sample is taken to be the inverse-time-distance weighted mean of the four nearest standard measurements

$$R_{std,i} = \frac{\frac{1}{\Delta t_1}R_{s1} + \frac{1}{\Delta t_2}R_{s2} + \frac{1}{\Delta t_3}R_{s3} + \frac{1}{\Delta t_4}R_{s4}}{\frac{1}{\Delta t_1} + \frac{1}{\Delta t_2} + \frac{1}{\Delta t_3} + \frac{1}{\Delta t_4}}, \tag{6}$$

where the nearest standard measurements are denoted by $s1, ..., s4$ and the $\Delta t_1, ..., \Delta t_4$ are the time differences between the measurement of the unknown sample and the measurements of the standards, e.g. $\Delta t_1 = |t_i - t_{s1}|$.

The correction for isotopic fractionation for a sample is done with the equation

$$R_{x[-25]} = R_{x[\delta]} \frac{1 - 25/1000}{1 + (\delta^{13}\mathrm{C})_x/1000}, \tag{7}$$

where the ratio is normalized to the δ^{13}C value in the square brackets and where $R_{x[\delta]}$ is the measured $^{14}\mathrm{C}/^{13}\mathrm{C}$ ratio.

The ^{14}C activity of the HOxII standard is related to the canonical modern activity (year 1950) by the equation [69]

$$A_{1950[-25]} = 0.7459\, A_{\mathrm{HOxII}[-25]}. \tag{8}$$

To better than one part in 10^4 the same holds for the $^{14}\mathrm{C}/^{13}\mathrm{C}$ ratio [70]

$$R_{1950[-25]} = 0.7459\, R_{\mathrm{HOxII}[-25]}. \tag{9}$$

The fraction modern $f_{x,j}$ value of measurement j of the sample x is now

$$f_{x,j} = \frac{R_{x,j[-25]}}{R_{1950[-25]}}, \tag{10}$$

and the fraction modern value for a sample is the mean of the fraction modern values of the measurements

$$f_x = \frac{1}{M_x}\sum_j f_{x,j}, \tag{11}$$

where M_x is the number of the measurements of sample x. The corresponding uncertainty estimate is the standard error of the mean

$$u_x = \sqrt{\frac{1}{M_x(M_x-1)}\sum_j (f_{x,j}-f_x)^2}. \tag{12}$$

Correcting the measured value for contamination, estimated from the measurement of a ^{14}C blank, f_b, the final fraction modern value is [70]

$$F_x = f_x(1+f_\mathrm{b}) - f_\mathrm{b}, \tag{13}$$

which assumes that the contamination is modern and that the sample masses are comparable. The uncertainty of F_x is given by

$$U_x = \sqrt{u_x^2(1+f_\mathrm{b})^2 + u_\mathrm{b}^2}. \tag{14}$$

From the fraction modern value in Eq. (13), one can calculate the conventional radiocarbon age

$$D_x = -8033\ \ln F_x, \tag{15}$$

which reflects the age of the sample and is given in years before the year 1950 (years Before Present, BP). However, because there are further intricacies in the radiocarbon method, the above estimate should be considered a conventional intermediate result, dependent only on the ^{14}C concentration of the sample. This emphasis is necessary because the atmospheric ^{14}C concentration has changed over time and the conventional radiocarbon age has to be calibrated to get the real age of the sample. Furthermore, the conventional radiocarbon age is calculated using the somewhat incorrect half-life of 5568 years, corresponding to the above-used Libby mean life $\tau = 8033$ years.

5 EXPERIMENTS AND RESULTS

The main purpose of the measurements in this work was to assess the performance of the Helsinki AMS. The results show that the modifications to the system have been successful and measurements to better than 1% accuracy are possible with the present system.

5.1 Stability and profiles

The sensitivity of the AMS results to changes in the accelerator system parameters is apparent from the plots in Figure 13 showing the measured quantities as functions of the important accelerator parameters. Subfigures (a) and (b) show the ^{14}C rate and the ^{13}C current as functions of the terminal voltage, while subfigures (c) and (d) show the ^{14}C rate as a function of the injector magnet field and the switching magnet field. The ^{13}C current was measured using GVM+CPU stabilization of the terminal voltage, whereas the other profiles were measured using Slit+CPU stabilization.

As noted previously, the terminal voltage is stable to better than 2 kV (peak to peak) at 3 MV, with a maximum rms deviation of 0.7 kV. For a Gaussian distribution with a FWHM equal to that of the profile in Figure 13, a 0.7 kV deviation from the centre would correspond to a 1.1% decrease in the ^{14}C rate. However, this deviation is an overestimate. Based on the present figure and other similar measurements, there is a roughly 5 kV-wide interval at the top of the profile where the ^{14}C rate remains constant. This means that the terminal voltage of the accelerator is sufficiently stable for ^{14}C measurements. Note that the 5 kV flat top in the profile also corresponds to the calculated effect of a 2.5 kV voltage deviation to the ion paths in the AMS beam line (see Figure 11).

The ^{13}C current, which is measured right after the analysing magnet, has a 8 kV-wide flat top in the profile, making it even less sensitive to changes in the terminal voltage than the ^{14}C rate.

The injector magnet field is reproducible and stable to 2×10^{-5} T, corresponding to a ^{14}C throughput change of 0.05% on the basis of the FWHM of the ^{14}C profile and Gaussian approximation. Hence, fluctuations in the injector magnet field are not likely to cause additional errors in the results. At present, the switching magnet field is not changed during the measurements. However, the profile shown in Figure 13(d) is relevant for monitoring the possible drift of the magnet's field.

5.2 Throughput

Table 3 lists the beam current of a 12.92 MeV $^{13}C^{3+}$ pilot beam in several Faraday cups along the beam line for measurements done in September 2007. On the basis of the 485 nA $^{12}C^{-}$ current in the injector, one expects a 5.3 nA $^{13}C^{-}$ current from the injector. The maximum yield for the 3^{+} charge state is roughly 55% (see Figure 4) and hence the maximum $^{13}C^{3+}$ current from the accelerator is 8.7 nA. A current of 8.3 nA was measured at the target, which necessitates at least

Table 3: Pertinent beam currents at different points of the beam line. At the injector, the ^{12}C current is given because the ^{13}C current is overlapped by a current from molecular ions.

Faraday cup	Beam current [nA]
Injector $M = 12$ u	485
Injector $M = 13$ u	43
Off-axis ^{13}C current	8.6
Cup before switching magnet ^{13}C	8.95
Detector ^{13}C	8.3

a 96% optical throughput. Also, the mean absolute $^{14}\mathrm{C}/^{13}\mathrm{C}$ ratio measured from HOxII standards was 1.516×10^{-10}, which is 97% of the maximum known 1.567×10^{-10}. The results agree nicely and are in accord with the ion optical calculations.

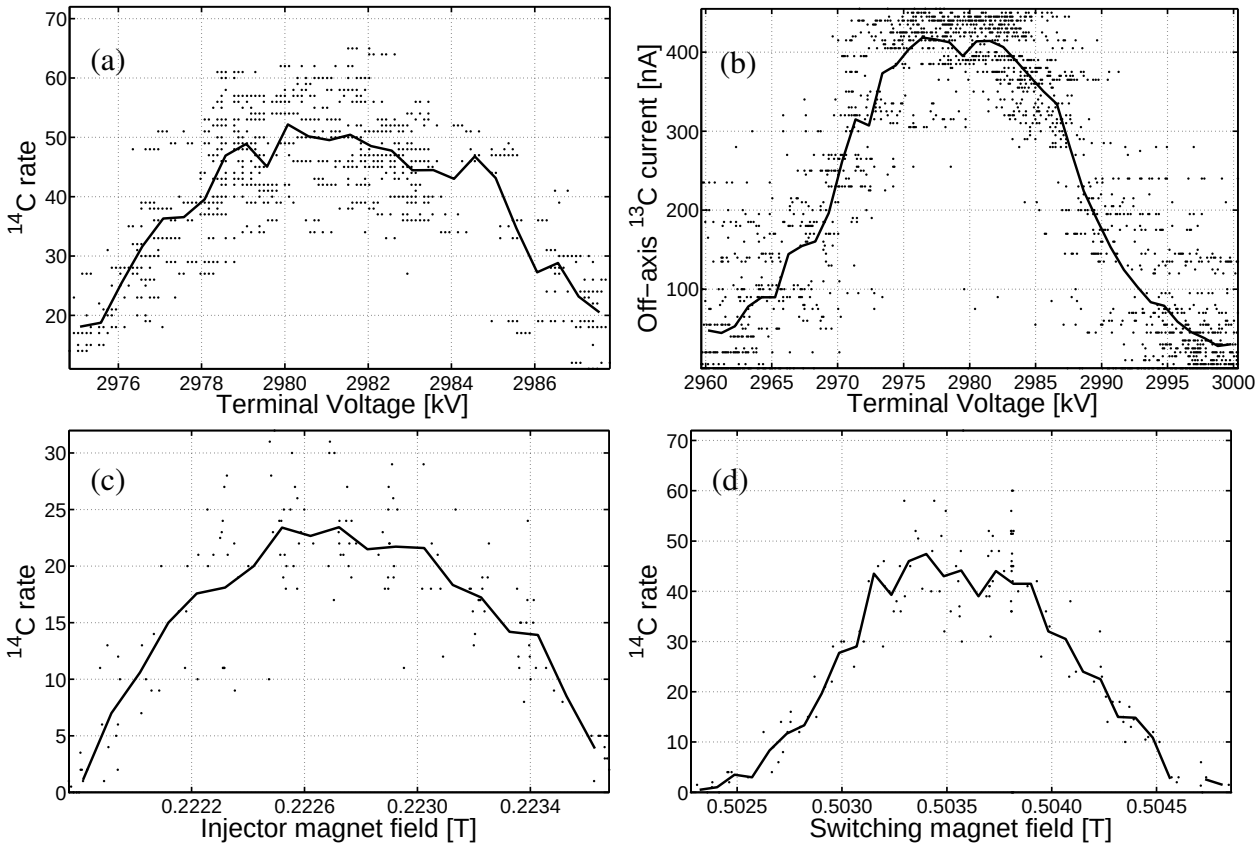

Figure 13: The throughput profiles for pertinent accelerator parameters. The dots show measured values. The curves represent mean values of measurements inside equally spaced bins.

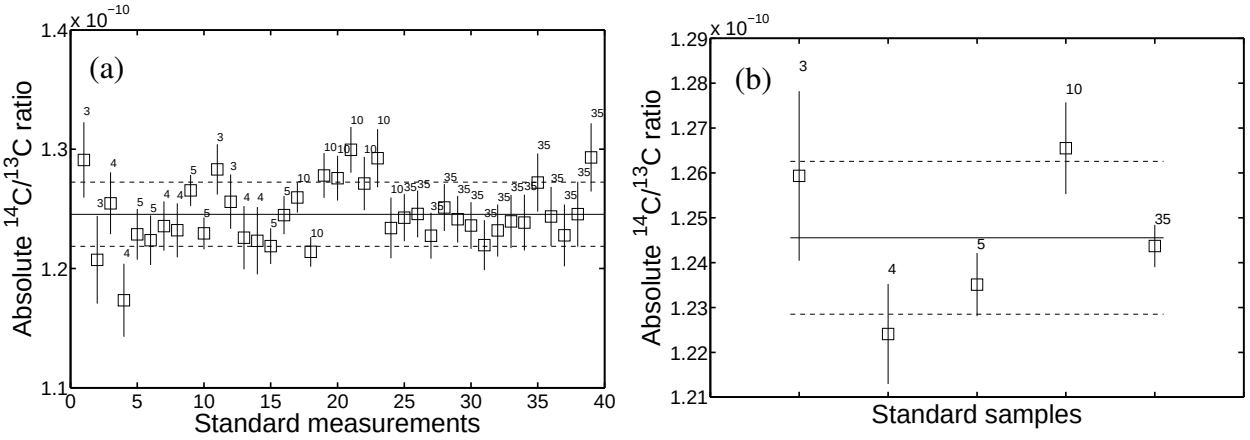

Figure 14: (a) Absolute $^{14}C/^{13}C$ ratios of individual measurements of five HOxII standards in one measurement run. The error bars represent the counting statistical uncertainties. The dashed lines show the 1σ interval. (b) Mean $^{14}C/^{13}C$ ratios for the standards in the measurement. The error bars represent the standard errors of the means.

5.3 Accuracy

Figure 14 shows the absolute ratios for one batch of (HOxII) standards, measured in October 2007. The results from individual measurements of the different samples agree nicely within the counting statistical errors. When the standard errors of the means are plotted for each sample, the agreement is tolerable. The relative between-sample standard deviation is 1.4%, whereas the average standard error of the mean is 0.8%. The average counting statistical error was 0.7%. The randomness inherent in sampling does not allow firm conclusions to be drawn on the basis of these numbers, especially because the uncertainties are not equal, but the results do suggest that additional error is present in the measurements. The measurements can be analysed further with the CAR model. The main results from the CAR model for the measurements are given here and the model itself is explained thoroughly in chapter 6.

Figure 15 gives the resulting pdfs (probability density functions) for the pertinent parameters of the CAR model. The parameters α and σ in Figure 15 represent roughly the correlation and the magnitude of the machine errors. These results indicate that an additional machine error is present and that the error is somewhat correlated, with the median of the correlation coefficient α being 7.8, resulting in an average correlation of 0.49 for the machine errors of nearby measurements. The median of the standard level change strength σ is 4.8×10^{-12}, which contributes on average a 1.1% uncertainty for each measurement in addition to the counting statistical uncertainty.

Table 4 gives the inferred ^{14}C concentrations and radiocarbon ages for measured samples of unknown ^{14}C concentration. It is seen that the overall uncertainties of the ^{14}C concentration are below 1% for the roughly modern samples. The available reference results agree rather nicely with the measured values.

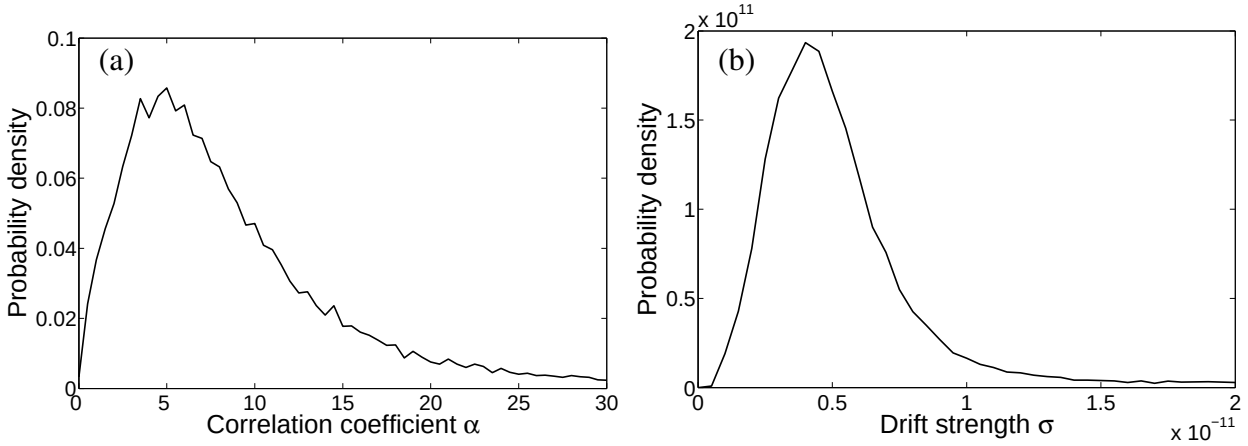

Figure 15: Some CAR results for an AMS run. (a) The inferred pdf for the correlation coefficient α. (b) The pdf for the CAR process strength σ.

Table 4: Measured ^{14}C concentrations and radiocarbon ages. Concentrations are given in per cents of the activity of modern carbon (pMC, see also Eq. 10). The value given is the median of posterior density, and the limits represent the 68.3% central posterior interval. Reference results from a well-established AMS laboratory were available for four samples. The uncertainties for the reference results represent a 1σ interval.

Sample	^{14}C concentration [pMC]	Radiocarbon age [BP]	Reference result [BP]
7	$26.52^{+0.34}_{-0.33}$	10660^{+100}_{-100}	10610 ± 75
8	$27.02^{+0.32}_{-0.31}$	10510^{+93}_{-93}	10435 ± 75
14	$92.66^{+0.93}_{-0.94}$	612^{+82}_{-80}	
15	$92.50^{+0.84}_{-0.86}$	627^{+75}_{-73}	
17	$65.89^{+0.66}_{-0.66}$	3351^{+80}_{-80}	3425 ± 35
18	$99.27^{+0.79}_{-0.79}$	59^{+64}_{-64}	
33	$67.33^{+0.54}_{-0.54}$	3177^{+65}_{-65}	
34	$67.03^{+0.56}_{-0.57}$	3213^{+68}_{-67}	3220 ± 40

Table 5: Measured ^{14}C concentrations and corresponding radiocarbon ages for different background materials. The value given is the median of posterior density, and the limits represent the 68.3% central posterior interval.

Sample	^{14}C concentr. [pMC]	Radiocarbon age [BP]	Reference [BP]
Anthracite, CO_2 LN cleaned two times	$0.79^{+0.083}_{-0.077}$	38880^{+810}_{-810}	
Antracite, ABA + combustion	$0.751^{+0.067}_{-0.063}$	39280^{+700}_{-700}	
Anthracite	$0.683^{+0.063}_{-0.059}$	40050^{+710}_{-720}	40300 ± 270
Anthracite, CO_2 LN cleaned three times	$0.534^{+0.054}_{-0.052}$	42020^{+810}_{-790}	
Industrial graphite	$0.495^{+0.057}_{-0.051}$	42630^{+850}_{-890}	42300 ± 1380
Industrial graphite, ABA	$0.482^{+0.058}_{-0.053}$	42850^{+920}_{-920}	
Graphite from VERA	$0.082^{+0.047}_{-0.034}$	57000^{+4200}_{-3700}	~ 57000
Ceylon graphite	$0.02^{+0.011}_{-0.009}$	68200^{+4200}_{-3600}	
Diamond, grey	$0.0045^{+0.0031}_{-0.0022}$	80300^{+5000}_{-4300}	
Diamond, white	$0.0033^{+0.0029}_{-0.0019}$	82600^{+6200}_{-5100}	

The results show that the Helsinki AMS is operational and able to reach a 1% or better accuracy for the measured concentration. In addition to the counting statistical error, there appears to be another error in the measurements. A likely source of such an additional error is the possible change of the ion source current between the measurements of the ^{14}C rate and the ^{13}C current.

5.4 Background

Because of the good vacuum conditions in the beam lines ($10^{-8} - 10^{-6}$ mbar), the two magnetic analysers, the electrostatic analyser and the long beam lines, the background of the AMS system is very low. The inclined fields of the accelerating tubes also filter out ions that undergo spurious charge changes in the tubes. As a result, it has been possible with the present setup to measure $^{14}C/^{12}C$ concentration values as low as 4×10^{-17} (without background subtraction).

As discussed in paper **V**, several types of background samples were prepared for AMS measurements as tests for both the sample treatment background and the AMS machine background. The analysis in paper **V** was done using uniform priors for the ^{14}C concentrations (the O_i parameters in the CAR model). Here the inverse square root prior was used instead. Table 5 gives the resulting medians of posterior density and the 68.3% central posterior intervals for the radicarbon concentrations and ages for the more interesting background samples. The results are in good agreement with the available reference results. The background of the spectrometer is very low, with the 80 ka BP values being among the lowest values reported [71] by AMS laboratories.

6 BAYESIAN ANALYSIS OF AMS DATA

6.1 Bayesian methods and radiocarbon

In most dating methods, not the age but the concentrations of isotopes are measured. The inference of the age from the concentration always involves assumptions. Often these assumptions concern starting concentrations, closed systems, and constancy of the rate of the underlying process. It should be remembered that uncertainties in quoted ages mostly represent uncertainties in the measurement of the concentration. Systematic errors due to violations of the assumptions in the method are not included in the final uncertainty estimate. To put this in Bayesian terms, all uncertainties are conditional on the model assumptions. A short introduction to Bayesian inference is given in Appendix B.

At the advent of radiocarbon dating, the atmospheric concentration was incorrectly assumed to be constant in accord with uniformitarianism. The half-life of 5568 years utilized in the calculations was also somewhat incorrect. When past atmospheric radiocarbon levels were made available, mainly from dendrochronologically dated tree rings, it was decided that, in order to enable comparison of dates and updating of results based on further changes in the calibration procedure, radiocarbon ages should be given in two parts: first, in radiocarbon years, using the year 1950 atmospheric radiocarbon level and the incorrect half-life, and second, in calibrated years, using the latest atmospheric radiocarbon data obtained from samples of known calendar age. The calibration means that the reliability of radiocarbon dating is dependent on other dating methods, most notably on dendrochronology. (On the other hand, dendrochronology is somewhat dependent on radiocarbon dating because radiocarbon is often used to pre-date floating chronologies.)

The radiocarbon calibration is inherently an inversion problem. Because of this and the fact that additional information (e.g., archaeological dates, stratigraphic order of samples) is often available for the samples, Bayesian probability theory has been a natural addition to the toolbox of radiocarbon researchers. Bayesian methods have been developed for radiocarbon calibration [72], for calibration curve construction [73, 74], for improving the precision of dates with the use of information about stratigraphic succession [75, 76], and for the detection of outlier dates [77].

I have taken the use of Bayesian methods in radiocarbon and AMS to two further areas, namely to the analysis of AMS measurement data and to the spectral analysis of the radiocarbon calibration data. The Bayesian models for the spectral analysis of atmospheric proxy data were developed first [78–80]. In brief, the method provides better estimates for the number of frequencies than do the methods utilizing confidence levels, which are dependent on assumptions about the noise and trend removal, often not made clear to other researchers. Other advantages of the Bayesian approach include the ability to take into account individual measurement uncertainties and the possibility to analyse unevenly sampled data. The method also offers better resolution and gives a clear view of the uncertainties of the period estimates since the output is a probability distribution. This is

helpful when comparing different proxies. Our main finding in applying the method is that there are no plausible frequencies in the radiocarbon calibration record. But for the sake of maintaining a single theme, the treatment of the spectral analysis model is not considered as part of this thesis. The reader interested in spectral analysis is encouraged to read my latest article [81] on this subject.

The novel CAR model presented below for the analysis of AMS measurement data was developed on the basis of the more general parts of the spectral analysis model, most notably the noise process and the inferential algorithm.

As already noted, because of the uncertainties concerning the sputtering process, charge exchange processes, and ion paths, the throughput of an AMS machine is not known to a sufficient accuracy. Obtaining accurate concentrations depends on the comparison of individual measurements to the measurements of known standards. However, the machine throughput may change between the measurement of the unknown sample and the standard. The proper normalization to the standard value is one consideration for AMS data analysis. Other considerations are the shape of the final probability density function (pdf) for the concentration and the reliability of the given uncertainty estimate.

Previous approaches to AMS data analysis include the different variations of the mean-based (MB) method [68, 82–84] and a likelihood-based approach [85]. The MB approach that I used was introduced in section 4.4.3. The method described in ref. [68] differs from mine mainly in that there the normalization to the standards is done after taking the mean of two nearby standard measurements, and the rather unstable uncertainty of the standard level is added quadratically to the uncertainty of the unknown sample. Because of this, the MB method used here is expected to yield better uncertainties. In considering the more general problem of how to take into account prior knowledge of the counting statistics when sampling-based estimates are used, Currie [82] compares four methods. The first method uses only the uncertainty from Poisson statistics, the second is roughly the MB presented here, the third uses the larger of the first and second methods' uncertainties [83], and the fourth scales the uncertainty of the third method down a bit. In that the first method is unrealistic and the last two methods are basically just provisional corrections to the second method, the MB method presented in section 4.4.3 would appear to be an appropriate and sufficiently simple foil to which to compare the novel Bayesian CAR model. The likelihood approach described in ref. [85] incorporates some of the advantages of the present Bayesian method but seems not to have been tested or developed further.

When the standard level does not appear to vary significantly during a measurement run, many AMS laboratories assume a constant standard level and normalize their results to the mean of the results of the standard measurements and use the standard error of the mean as the standard level uncertainty. This special case of the MB method will be termed MBCSL (Mean-Based method with Constant Standard Level). Where relevant, the CAR model will also be compared with the MBCSL method.

As is usual with non-Bayesian methods, the MB method makes assumptions that are not entirely transparent. Among these is the assumption that the standard error represents the real scatter, which will not be the case, however, if the values are correlated due, for example, to machine drift or the use of the same standard measurements for normalization. The final distribution is often assumed to be Gaussian in order to enable easy use of standard error. But because the standard error is not known in advance, the mean will have a Student's t-distribution, which is usually sufficiently well approximated with a Gaussian pdf only when the number of measurements is about 10 or more. Normalization with the measured values of the standards also gives a slightly non-Gaussian contribution.

There is, moreover, also more information in the measurement data than is used by the MB approach. Five points can be noted. First, variations in the measurements for each sample tell something about machine uncertainty, provided that the counting statistical uncertainty is properly taken into account. Machine uncertainty can then be used with the counting statistical uncertainty to give more reliable uncertainties when the number of measurements per sample is small. This way, even a sample that can be measured only once can be given an uncertainty that also has a contribution from the machine drift. Second, with less than ten measurements it will often be the case that the standard deviation of the mean happens to be either too small or too large, resulting in unreliable uncertainties for the MB approach. Rather than separating the known counting statistical uncertainty and the standard error of the sample mean and using one or the other, it would be better to combine scatter in the measurements with the known counting statistical uncertainty. Third, to the extent that the machine drift is a slowly-varying function of time, not only the comparison of the present and standard sample but also the measurements of nearby samples tell something about the ^{14}C concentration of the present sample. Fourth, an AMS machine is often stable enough for use of a constant standard level, but not always. The decision on how to use the standards should also be made probabilistically, on the basis of all relevant information. Fifth, some of the MB methods do not give or use the uncertainty of the interpolated standard level. It would be preferable to handle the standard level probabilistically, so making possible the use and inspection of the uncertainty of the standard level.

On the basis of the above considerations, a novel higher-level data-analysis model was developed. The model describes the standard level with a continuous autoregressive (CAR) process, which will be defined in the next section. After the autoregressive process has been introduced, the basic core of the new CAR model will be described. The δ^{13}C and background corrections will be introduced only later, as modifications to the basic model. This will make the main discussion simpler and independent of the peculiarities of radiocarbon dating.

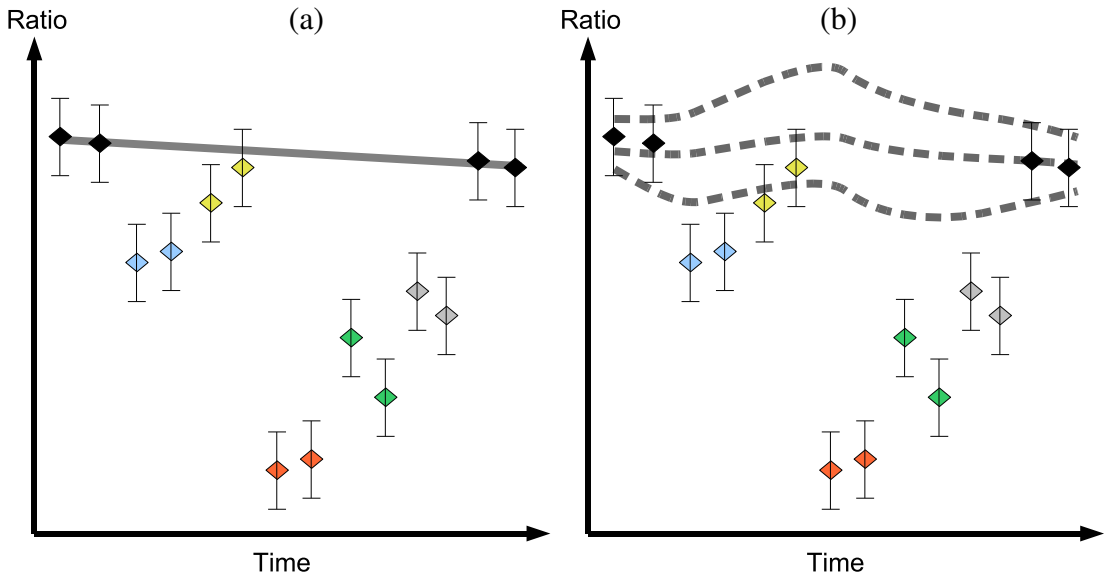

Figure 16: Two ways of interpolating a varying standard level. The black symbols represent the measurements of standards, the other colours the measurements of unknown samples. (a) Variants of the MB method typically use the mean of nearby standard measurements or use linear interpolation between the standards. More distant standards may or may not be used. If uncertainties are given at all, they do not increase when going farther away from the standards. (b) The CAR method assumes a probabilistic process for the standard level, which adapts itself to the measurements at hand. Uncertainties and the proper use of the standards farther away are determined by the measurements. Multiple measurements of unknown samples can also be used to track some of the changes in the standard level.

6.2 Autoregressive processes

As noted above, the novel Bayesian model uses a continuous autoregressive process to describe the standard level. The process can be thought of roughly as continuous-time random walk. Figure 16 shows the difference between the handling of the standard level in the MB method and the present new CAR model.

A discrete-time autoregressive time series is generated by the following equation [86]:

$$y_j = \phi y_{j-1} + \eta_j, \tag{16}$$

where η_j is a sequence of uncorrelated identically distributed random variables. The CAR process is a generalization of the above discretely sampled process to the continuous time domain. The mathematical model for this process is

$$\frac{\mathrm{d}}{\mathrm{d}t}x(t) + \alpha x(t) = \sigma\eta(t), \tag{17}$$

where $\sigma \in [0,\infty[$ mainly describes the strength of the changes in the CAR process per unit time and $\eta(t)$ is the derivative of a unit variance Wiener process (continuous-time random walk process).

The Wiener process $W(t)$ has $W(t_1) - W(t_2) \sim N(0,\ |t_1 - t_2|)$. The correlation coefficient $\alpha \in [0, \infty[$ is small for a highly correlated process. It can be shown [86] that the CAR process has the conditional mean

$$\mathrm{E}\,[x(t_2)|x(t_1)] = e^{-\alpha(t_2-t_1)}x(t_1), \tag{18}$$

and the variance

$$\mathrm{var}\,[x(t_2)|x(t_1)] = \frac{\sigma^2}{2\alpha}[1 - e^{-2\alpha(t_2-t_1)}]. \tag{19}$$

Hence, a useful difference equation is [87]

$$x(t_i) = x(t_{i-1})e^{-\alpha\Delta t_i} + \nu_i, \tag{20}$$

where $\Delta t_i = t_i - t_{i-1}$ and $\nu_i \sim N(0,\ \frac{1-\mathrm{e}^{-2\alpha\Delta t_i}}{2\alpha}\ \sigma^2)$.

The above equations of the CAR process leave open the probability of the first (or the last) point. To enable the compatibility with white noise for the first point, we take the fist point to be distributed as

$$x(t_1) \sim N(0, \sigma^2/2\alpha). \tag{21}$$

6.3 CAR model for data analysis

We will represent the N measured ^{14}C count to ^{13}C current ratios with a vector $\mathbf{R} = (R_1, R_2, \ldots, R_N)$ with corresponding measurement times $\mathbf{T} = (t_1, \ldots, t_N)$. By $\mathbf{I} = (I_1, \ldots, I_N)$ we will denote the corresponding ^{13}C currents, and by $\boldsymbol{\tau} = (\tau_1, \ldots, \tau_N)$ the corresponding ^{14}C counting time intervals (durations). The number of samples in the measurement will be denoted by M, and the parameters $\mathbf{O} = (O_1, \ldots, O_M)^{\mathrm{T}}$ will represent the true unknown fraction modern values for each sample, the inference of which is the goal of our analysis. The function $n(i)$ gives the corresponding sample number for each measurement i.

Let $\mathbf{L} = (L_1, \ldots, L_N)$ be the standard level (or throughput) including a sufficient constant for unit conversion from radiocarbon concentrations to measured ratios. The standard level is assumed to follow a CAR(1) process $x(t)$ around a mean m,

$$L_i = x(t_i) + m. \tag{22}$$

Now, given the standard level and the radiocarbon concentration of a sample, the expected number of counts in a single measurement of the sample is $\lambda_i = O_{n(i)}L_iI_i\tau_i$, which is also the mean of the Poisson distribution for the ^{14}C counts. On the other hand, the measured number of counts is, from the measurements, $c_i = R_iI_i\tau_i$. The predicting probability for the measured isotope ratio is, from the Poisson distribution for the ^{14}C counts,

$$p(R_i|O_{n(i)}, L_i) = I_i\tau_i\frac{e^{-\lambda_i}\lambda_i^{c_i}}{c_i!}. \tag{23}$$

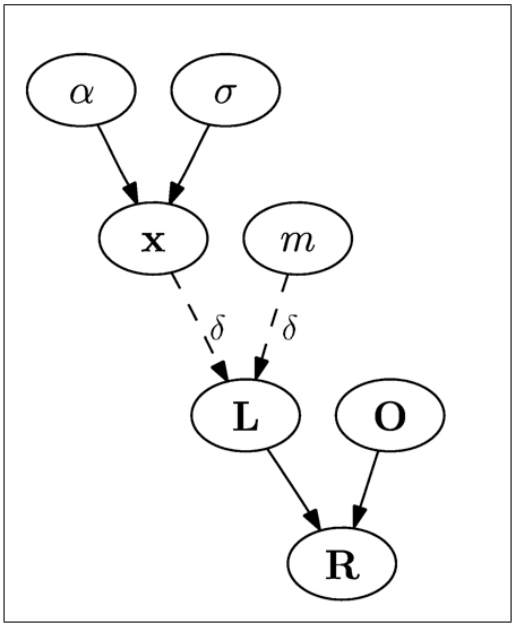

Figure 17: The hierarchy of the different parameters in the model. Solid arrows represent directional probabilistic dependencies between the parameters. A deterministic dependency is represented with a dashed line and a symbol δ, which denotes the Dirac delta function. In general, when writing down the terms in the joint pdf, the parameter at the arrow's source (parent) is needed as background information in the pdf for the arrow's target parameter (child) [88].

Note that Eq. (23) represents the known counting statistical uncertainty in the measurements. The other possible errors are described with the CAR process. The parameter α describes the type and the parameter σ the magnitude of the additional sources of error.

From Eq. (20) we get the probability density for $x(t)$. Denoting $\mathbf{x} = (x(t_1), \ldots, x(t_N))$ we have

$$p(\mathbf{x}|\alpha,\sigma) = \prod_{i=1}^{N} \frac{\sqrt{\alpha}}{\sqrt{\pi(1-e^{-2\alpha\Delta t_i})}\sigma} \exp\left(-\frac{\alpha(x_i - e^{-\alpha\Delta t_i}x_{i-1})^2}{(1-e^{-2\alpha\Delta t_i})\sigma^2}\right). \tag{24}$$

Figure 17 shows the hierarchy of the different parameters of the model.

6.3.1 Priors

Table 6 gives the priors used in the model. Independent one-parameter Jeffreys-rule priors are used for the most important parameters O_i, the derivation of which is shown below.

Jeffrey-rule priors have been found to perform well in most situations [89]. The rationale behind the Jeffreys-rule prior is that two persons using different parametrizations of the problem should get the same posterior probability [90]. This consideration leads to the prior being proportional to

Table 6: Priors for the model parameters. Prior ranges are limited to positive values. The ^{14}C concentrations of the standard samples are known. For example, when using ^{13}C -currents and HOxII standards, $F_s = 1.3407$ fraction modern and $\sigma_s \approx 10^{-4}$.

Parameter	Symbol	Prior type
CAR correlation coefficient	α	uniform
CAR standard deviation	σ	σ^{-1}
Standard level mean	m	uniform
Sample fraction modern	O_i	$1/\sqrt{O_i}$
Standard fraction modern	O_i	$N(F_s, \sigma_s^2)$

the square root of the determinant of the Fisher information matrix [90–92], defined as

$$J_{\mathbf{\Theta}} = -\mathrm{E}_{\mathbf{y}}\left[\frac{\partial^2 \ln(p(\mathbf{y}|\mathbf{\Theta}))}{\partial\Theta_i\,\partial\Theta_j}\right], \tag{25}$$

where $\mathbf{y}$ is the vector of the data values and $\mathbf{\Theta}$ a vector of the model parameters.

The prior for O_i can be calculated from the likelihood in Eq. (23). Dropping the subscript i, we have

$$L = \ln(p(c|\lambda)) = -\lambda + c\ln\lambda - \ln(c!) \tag{26}$$

for $c >> 1$. Now

$$\frac{\partial^2 L}{\partial\lambda^2} = -c/\lambda^2. \tag{27}$$

The Fisher information matrix is

$$J_\lambda = -\mathrm{E}_c\left[\frac{\partial^2 L}{\partial\lambda^2}\right] = \sum_{c=0}^{\infty}\frac{c}{\lambda^2}\frac{e^{-\lambda}\lambda^c}{c!} = \frac{e^{-\lambda}}{\lambda^2}\sum_{c=0}^{\infty}\frac{c\lambda^c}{c!} = \lambda^{-1}. \tag{28}$$

And the prior is

$$p(\lambda) \propto \sqrt{J_\lambda} = \lambda^{-1/2}. \tag{29}$$

Since we are holding the other parameters constant, $O_i \propto \lambda$, resulting in $p(O_i) \propto O_i^{-1/2}$.

6.3.2 Posterior

We now have both the probabilistic relations (the arrows) between the entities in Figure 17 and the prior probabilities for the parameters without parents. Using the chain rule for belief networks [88]), we can write down the joint pdf for all the parameters and data: $p(\alpha,\sigma,m,\mathbf{O},\mathbf{x},\mathbf{R}) = p(\alpha,\sigma,m,\mathbf{O})p(\mathbf{x}|\alpha,\sigma)p(\mathbf{R}|m,\mathbf{O},\mathbf{x})$. We are interested in the probability for all the parameters

given the data, or the posterior probability, which can be obtained from the joint pdf by using the product rule of probability, $p(\mathrm{A},\mathrm{B}) = p(\mathrm{A}|\mathrm{B})p(\mathrm{B}) \Leftrightarrow p(\mathrm{A}|\mathrm{B}) = p(\mathrm{A},\mathrm{B})/p(\mathrm{B})$. Thus

$$
\begin{aligned}
p(\alpha,\sigma,m,\mathbf{O},\mathbf{x}|\mathbf{R}) &= \frac{p(\alpha,\sigma,m,\mathbf{O},\mathbf{x},\mathbf{R})}{p(\mathbf{R})} \\
&= \frac{p(\alpha,\sigma,m,\mathbf{O})p(\mathbf{x}|\alpha,\sigma)p(\mathbf{R}|m,\mathbf{O},\mathbf{x})}{p(\mathbf{R})} \\
&\propto \frac{1}{\sigma}\prod_s \exp\left(\frac{-(O_s-F_s)^2}{2\sigma_s^2}\right)\prod_i \frac{1}{\sqrt{O_i}} \\
&\times \prod_{i=1}^{N} \frac{\sqrt{\alpha}}{\sigma\sqrt{1-e^{-2\alpha\Delta t_i}}} \exp\left(\frac{-\alpha(x_i - e^{-\alpha\Delta t_i}x_{i-1})^2}{(1-e^{-2\alpha\Delta t_i})\sigma^2}\right) \\
&\times \prod_{j=1}^{M} e^{-\lambda_j}\lambda_j^{c_j},
\end{aligned}
\tag{30}
$$

where in the third line we have dropped the marginalization constant $p(\mathbf{R})$ and other constants because these are not relevant for the inferential algorithm. The first product in Eq. (30) is the product of the priors of the standard samples (see table 6). F_s is the known fraction modern value of the standard and σ_s is the uncertainty of the standard value. This product fixes the value of the CAR process at the points of standard measurements.

6.4 Computation

Inferences from the posterior are made with a Markov Chain Monte Carlo (MCMC) algorithm [93], which gives parameter space points distributed according to the posterior given in Eq. (30). An adaptive Metropolis-Gibbs hybrid sampler was used in this work. The algorithm uses Metropolis steps with different guessing distributions. For the trend parameters x_i these are approximated full conditional distributions (the Gibbs part). The guessing distributions for the other parameters are drawn from adaptive normal distributions.

The convergence of the MCMC chain to the target pdf can be checked both by looking visually at the trace plots and by using the PSRF and MPRSF convergence diagnostics developed by Gelman and Rubin [94, 95]. Ready packages for implementing these methods are MCMCDIAG [96] for MATLAB and BOA [97] for R. The main idea is that multiple independent chains with random starting values are simulated, and their total posterior variance and the within-chain variance are compared. A value near unity for the ratio $\hat{R}$ of the variances is taken to be a signal for convergence. In this work the common constraint $\hat{R} < 1.2$ is used as the requirement for convergence. A convergence plot using six chains for the analysis of background sample measurements is shown in Figure 18. With the present code, convergence is typically attained after a burn-in of 10^7 MCMC points, which takes less than an hour per chain on a modern 2 GHz PC.

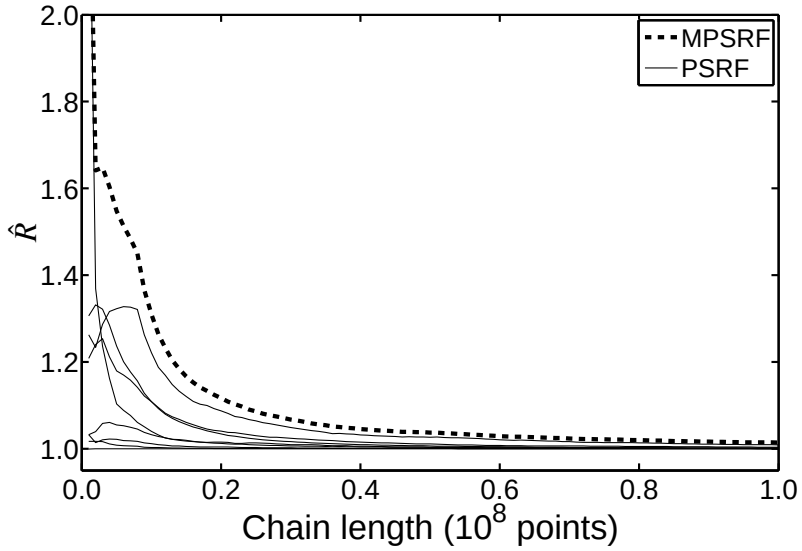

Figure 18: MPSRF (thick dashed line) and PSRF (thin lines) convergence diagnostics for a typical measurement analysis run. PSRF lines are drawn for the parameters α, σ, m and for two O_i's and x_i's. Convergence is taken to be attained when $\hat{R} < 1.2$.

6.5 δ^{13}C correction

As mentioned in section 4.4.3, in addition to the radioactive decay of ^{14}C, there are other processes in nature that may slightly change the relative amounts of carbon isotopes in the sample. These changes are referred to as fractionation. For ^{14}C, fractionation is corrected by measuring how much the isotope ^{13}C has fractionated and correcting ^{14}C accordingly. For the ^{14}C/^{13}C ratio the correction is linear (see Eq. (7) in section 4.4.3). Typically the correction is some per mils, roughly of the same order as the typical uncertainty of the AMS measurement. The relative uncertainty of the measured δ^{13}C value is typically less than a per cent and can be ignored in the present discussion.

To show how the fractionation correction should be done when using the CAR model, we will extend the definition of $\mathbf{L}$, the changing standard level, to include all fractionation between the atmospheric concentration and the measurement. Total change is then a product of the fractionation seen in the δ^{13}C value and other fractionation, $L_{\mathrm{tot},i} = L_{13,i}L_i$. We will denote this extension the $\mathrm{CAR_{LL}}$ model. The expected number of counts in a measurement is now

$$\lambda_i = O_i L_{\mathrm{tot},i} I_i \tau_i = O_i L_{13,i} L_i I_i \tau_i. \tag{31}$$

The value of the δ^{13}C fractionation $L_{13,i}$ is the inverse of its correction in Eq. (7) in section 4.4.3, namely

$$L_{13,i} = \frac{1 + (\delta^{13}\mathrm{C})_\mathrm{i}/1000}{1 - 25/1000}. \tag{32}$$

In the $\mathrm{CAR_{LL}}$ model the likelihood of the measurement depends only on

$$\lambda_i = O_i L_{13,i} L_i I_i \tau_i = O_i L_i I_i^* \tau_i, \tag{33}$$

and

$$c_i = R_i I_i \tau_i = R_i^* I_i^* \tau_i, \tag{34}$$

where we use the transformations

$$\begin{aligned} R_i^* &= L_{13,i}^{-1} R_i, \text{and} \\ I_i^* &= L_{13,i} I_i. \end{aligned} \tag{35}$$

Because the data enters the posterior (Eq. (30) above) only through the λ_i's and c_i's, the $\mathrm{CAR_{LL}}$ model is equivalent to the CAR model with the above $\mathbf{R}^*$ and $\mathbf{I}^*$ as data.

Hence, because the $L_{13,i}$ values are known and we will not take their uncertainty explicitly into account, it is possible to take the known fractionation correctly into account with the conceptually simpler model of section 6.3 by transforming the data by Eqs. (35) prior to analysis.

6.6 Background correction

An important part of an AMS result for an old sample is the control for ^{14}C background coming from the treatment of the sample before the measurement and from the AMS machine itself. Each AMS sample wheel typically contains a couple of samples representing different types of background. This section explains how to infer the intrinsic ^{14}C content of the other samples from the measurements of the background samples. We will first extend the CAR model to take different background contributions into account with explicit parameters in the general case and then offer a simpler and more restricted solution sufficient for a typical AMS measurement.

6.6.1 Rigorous method for background correction

Sample contamination in AMS samples is typically mass dependent [70], with less than a microgram of modern carbon being introduced to the sample during the sample preparation. A constant background independent of the sample mass is also possible. Because different types of samples undergo different sample treatments before analysis, the samples may have somewhat different sources of background, which means that it may be necessary to assign different contamination parameters to them. Let $\mathbf{C} = (C_1, \ldots, C_M)^{\mathrm{T}}$ represent the total ^{14}C concentrations in the samples with masses $\mathbf{m} = (m_1, \ldots, m_M)$ and let the vector $\mathbf{O}$ represent the intrinsic ^{14}C concentrations. The expected number of counts for a measurement is then $\lambda_i = C_{n(i)} L_i I_i \tau_i$. Contributions from the different background sources can be represented with sums of the form

$$C_i = \left(\frac{m_i - \sum_j u_j}{m_i} \right) O_i + \sum_j \left(\frac{u_j}{m_i} \right) o_j + \sum_j b_j, \tag{36}$$

where the different mass-dependent contaminations are represented with masses $\mathbf{u} = (u_1, ..., u_l)$ and ^{14}C concentrations $\mathbf{o} = (o_1, ..., o_l)$ and the constant background contributions are represented with $\mathbf{b} = (b_1, ..., b_h)^{\mathrm{T}}$. The above sums can be given for the whole concentration vector as

$$\mathbf{C} = (I - \Gamma U)\,\mathbf{O} + \Gamma A\mathbf{v} + B\mathbf{b}, \tag{37}$$

where the matrices A and B consist of zeros and ones and represent the user-given assignments of the different background sources for each sample. The matrix U has the elements $U_{ij} = \delta_{ij}\sum_k A_{ik}u_k$ and the vector $\mathbf{v}$ the components $v_i = u_i o_i$. I is an identity matrix and Γ a diagonal matrix of the inverse masses of the samples. With the above addition to the CAR model, a well-defined and flexible probabilistic background subtraction method is available.

6.6.2 Approximate method for background correction

The AMS researcher may want to test different combinations of the background samples, which can be done faster by introducing the additional information about the background samples only after the CAR analysis. In this case the $\mathbf{O}$ obtained from the MCMC run represents the total ^{14}C concentrations in the samples. Let $\mathbf{W} = (W_1, \ldots, W_M)^{\mathrm{T}}$ be a new parametrization of the sample ^{14}C concentrations, representing the intrinsic ^{14}C concentrations for most samples and the contaminant masses for the background samples. In this case the number of parameters remains the same, and a $M \times M$ matrix K describes the relationships between the samples

$$\mathbf{O} = K\mathbf{W}. \tag{38}$$

Often there is additional information concerning the W_i. For example, they are all non-negative. Call this information $\mathrm{I_P}$. From the CAR analysis we have $p(\mathbf{O}|\mathbf{R})$ and hence we also have $p(\mathbf{W}|\mathbf{R}) = p(\mathbf{O}|\mathbf{R})\left|\frac{\partial(W_i,\ldots,W_M)}{\partial(O_i,\ldots,O_M)}\right| = \frac{1}{|K|}p(\mathbf{O}|\mathbf{R})$. We want

$$\begin{aligned} p(\mathbf{W}|\mathbf{R},\mathrm{I_P}) &= \frac{p(\mathbf{W},\mathrm{I_P}|\mathbf{R})}{p(\mathrm{I_P}|\mathbf{R})} = \frac{p(\mathbf{W}|\mathbf{R})p(\mathrm{I_P}|\mathbf{W},\mathbf{R})}{p(\mathrm{I_P}|\mathbf{R})} \\ &= \frac{p(\mathbf{O}|\mathbf{R})p(\mathrm{I_P}|\mathbf{W},\mathbf{R})}{|K|p(\mathrm{I_P}|\mathbf{R})} \propto p(\mathbf{O}|\mathbf{R})p(\mathrm{I_P}|\mathbf{W},\mathbf{R}). \end{aligned} \tag{39}$$

Because $p(\mathrm{I_P}|\mathbf{W},\mathbf{R})$ has the value one when the W_i are nonzero and zero otherwise, $p(\mathbf{W}|\mathbf{R},\mathrm{I_P})$ can be obtained from the MCMC chain of $p(\mathbf{O}|\mathbf{R})$ by calculating corresponding $\mathbf{W}$ for each $\mathbf{O}$ and dropping out points where any of the calculated W_i do not satisfy $\mathrm{I_P}$ (i.e. are negative). Note, however, that the above assumes that the determinant of K is nonzero. The background correction with Eq. (38) is only an approximation, however, because the priors in the CAR analysis were defined for the O_i and hence the values of the standards were enforced to their fraction modern values without background correction. The small error can be corrected approximately by multiplying all resulting intrinsic ^{14}C concentrations (W_i) by the factor $\frac{\langle O_s\rangle}{\langle W_s\rangle}$, which for 1μg/1mg modern contamination and HOxII standards is 1.00025, corresponding to a -2 year correction to the dates.

In most AMS measurements one background sample is sufficient for all samples measured at one time. Furthermore, the samples usually have comparable masses m, and the ^{14}C concentration o of the contamination is known from previous measurements. If a constant mass u of the contaminant is assumed to be incorporated into all samples during sample preparation, taking $W_b = u$, equation (38) becomes

$$\mathbf{O} = \left(1 - \frac{u}{m}\right) E\mathbf{W} + \frac{o}{m} D\mathbf{W}, \tag{40}$$

where E is an $M \times M$ identity matrix, except for the row b which is filled with zeros, and where D is an $M \times M$ matrix of zeros, except for the column b which is filled with ones. Note that the intrinsic ^{14}C concentration of the blank was assumed to be zero. For each sample, the intrinsic ^{14}C concentration from Eq. (40) is then

$$W_i = \left(1 - \frac{u}{m}\right)^{-1} \left(O_i - \frac{ou}{m}\right), \text{ for } i \neq b. \tag{41}$$

The pdf for the W_i's can be obtained directly from the MCMC chain of the simple CAR model by using Eq. (41) for each point in the chain.

7 IMPROVED ACCURACY AND PRECISION

Different kinds of measurement data were simulated in order to compare the new Bayesian CAR model with a conventional mean-based method (MB method). First, data was simulated for increasing machine instability and hence increasingly large changes in the standard level. Second, measurements which use the same standard values were simulated in order to see the effect of correlations within the individual measurements of a given sample. Third, data for very old samples was simulated. Fourth, the number of measurements per sample was varied.

7.1 Minimally correlated AMS measurements

To assess the effect of increasing machine error with the MB, MBCSL, and CAR data-analysis methods, measurements with only one measurement per sample between standards were simulated. In the case of the MB method, when there is only one measurement per sample between the standard measurements, each measurement is normalized using independent standard values, minimizing correlations between the values used to calculate the mean and the error of the mean. This choice therefore represents the best-performance scenario for MB.

Each simulated measurement was drawn from a Poisson distribution whose expectation value was a product of the known ^{14}C concentration and Gaussian $\mathrm{AR}_{\alpha=1}$ (random walk) noise representing the drift. Six measurements were simulated per sample and nine unknown samples were measured once between standard samples. Altogether $40 \times 6 \times 4000$ measurements were simulated with MATLAB for each trend strength. Each run was analysed with the MB method. Because the analysis time for the CAR model is long, only $40 \times 6 \times 30$ of the simulated measurements for each trend strength were analysed with the CAR model. The trend strength value is the standard deviation of the change in standard level between two measurements relative to the true standard value.

Figure 19 shows the means of true errors in the ^{14}C concentrations given by each method as a function of increasing machine drift. Here, the CAR analysis was done with a uniform prior for the O_i. It is seen that, for the no-drift case, the CAR model is more accurate than the MB method and as accurate as the MBCSL method. With increasing drift the errors made by the MBCSL method increase dramatically while the CAR model continues to give accurate results.

7.2 Correlated AMS measurements

Figure 20 shows the mean true deviations and the fractions of points outside the quoted uncertainties for the CAR, MB, and MBCSL methods for correlated measurements (paper **IV**). Here, each unknown sample was measured twice before changing to the next sample. As already noted, the use of the same standard measurements introduces correlations to the normalized ratios. The MB

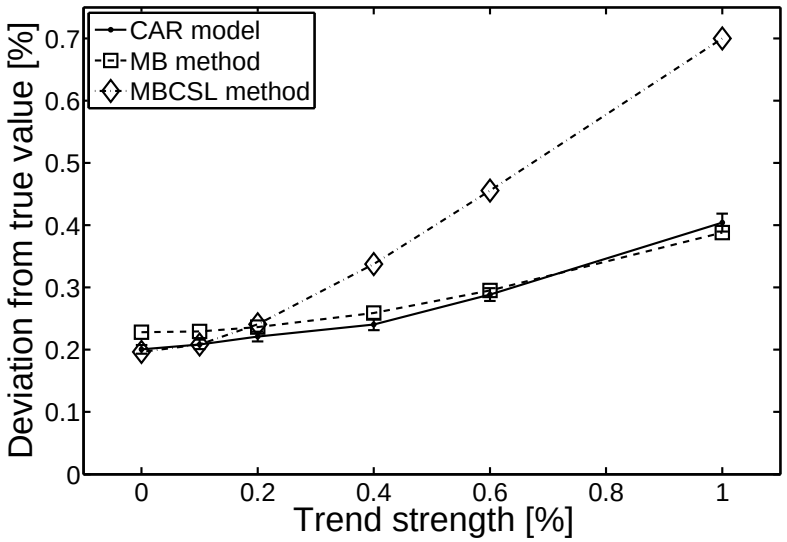

Figure 19: The means of absolute values of the differences between a method's results and the known true concentration as a function of increasing machine drift. The measurements were simulated for modern samples. The CAR model is more accurate than the MB method for a typical run of a modern high-precision AMS. In the optimal case, the MBCSL method is as accurate as the CAR model.

method makes the implicit assumption of no correlations when the standard error of the mean is interpreted to describe the deviation from the true concentration. For the present data the assumption does not hold and unreliable uncertainties result. Because the CAR model uses the whole measurement run as data, it takes the correlations into account naturally, giving reliable uncertainties. Again, the CAR analyses were done with a uniform prior for the O_i.

7.3 Bias and the choice of a point estimate

The effect of the prior is largest when the likelihood is broad. When the likelihood does not constrain the value of the parameter in question, the job is left more to the prior. With this in mind, test was made of the CAR model with three different reasonable priors for the essential parameters O_i and very old samples.

One obtains pdfs when using the CAR model. When it comes to reporting results, comparing the results of one method with another, or comparing priors used, there will often be a need to give a single number representing a good choice for the parameter. What is the best point estimate? This question has been dealt with elsewhere [91, 98], but, in short, the median of a pdf minimizes the absolute value of the error, the mean minimizes the squared error, and the point of maximum probability density is appropriate when only the correct result is of any worth. It is also widely known that whereas the mean tends to be sensitive to long tails (or outliers), the median is rather

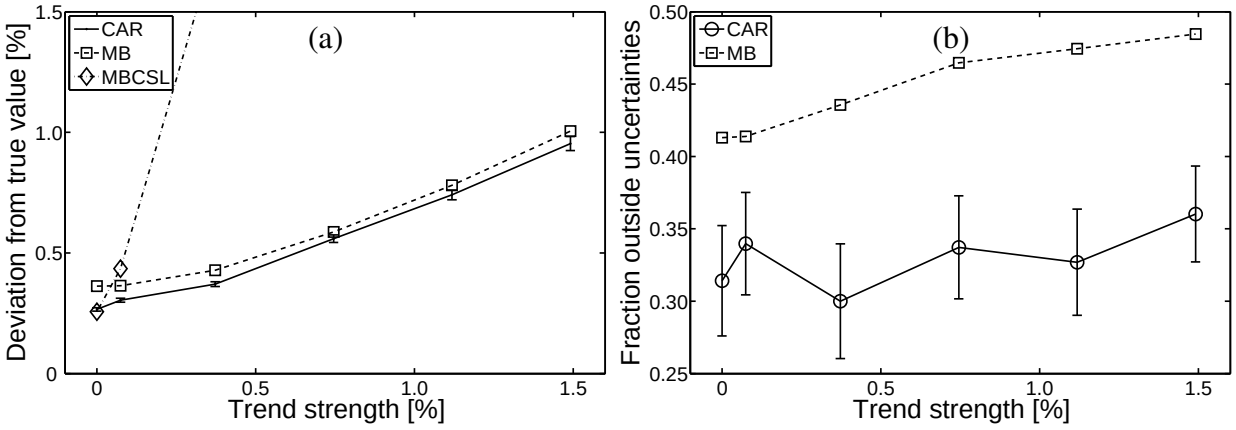

Figure 20: (a) Mean deviations from the true concentration for the CAR, MB, and MBCSL methods when two nearby measurements of a given sample use the same standard measurements for normalization. (b) The fraction of true concentration values outside the quoted uncertainties for CAR and MB for the correlated case. A 68.3% central posterior interval was used for CAR and a 1σ interval for MB. (Uncertainties for CAR were calculated from the corresponding binomial distribution.)

robust.

Contrary to some prominent Bayesians, who claim that the concept of bias has nothing to do with Bayesian analysis [98], I take the view that, while it is true that prior knowledge (and hence the prior) should affect the result of an analysis, considerations about the bias can serve as a check that the selected prior has not brought unwanted information into the analysis. In view of this, the priors were compared on the basis of bias and accuracy of the results.

Table 7 lists several combinations of the prior and point estimates. It is seen that the combination arrived at theoretically ($1/\sqrt{O_i}$ prior and the median) also performs best in the comparison. Thus, the Jeffreys-rule prior and the median as the point estimate are recommended for use with CAR. This combination is also used in the following sections.

The radiocarbon dater often needs good estimates for both the concentration and the conventional radiocarbon date. In this regard it is beneficial that the median and the central posterior interval are invariant under a change of variables. Note also that the use of the Jeffreys-rule prior results in the same posterior irrespective of the parametrization [89].

7.4 Old samples

To ascertain the performance of the methods for old samples, no-drift measurements of old samples were simulated and analysed by the MB and CAR methods.

Figure 21(a) shows the means of relative deviations between each method's results and the known

Table 7: Accuracies and biases of different combinations of the prior and the type of point estimate. MB results are included for comparison. The values are averages over the mean number of counts in the simulated measurements (0.1, 0.5, 1.0, 1.5, 2.0, 3.5, 5.0, or 10, see Figure 21). For MB, samples with zero counts were left out of the calculations relevant to age because an infinite age would have been obtained, resulting in an infinite bias.

Combination Prior, point estimate	Concentration deviation [10^{-4} pMC]	Concentr. bias [10^{-4} pMC]	Age deviation [ka BP]	Age bias [ka BP]
$1/O_i$, MP	28.0	-9.2	9.2	7.2
$1/O_i$, median	26.8	-3.8	7.1	5.5
$1/O_i$, mean	26.6	-1.0	7.1	5.7
$1/\sqrt{O_i}$, MP	26.0	-1.2	2.39	-0.60
$1/\sqrt{O_i}$, median	25.7	4.2	2.63	0.12
$1/\sqrt{O_i}$, mean	26.2	7.2	2.83	0.56
Uniform, MP	27.1	0.2	2.53	-1.34
Uniform, median	27.3	6.4	2.27	-0.84
Uniform, mean	28.1	9.5	2.21	-0.55
MB	27.7	0.0	2.66	-0.54

true values as a function of the mean of the total counts from the sample. The median was used as a point estimate for CAR. MBCSL is not included because the uncertainty from the counting statistics is much larger than the error from the handling of the standard level. Considering point estimates, the two methods seem to be equally accurate for old samples. However, point estimates are not the best way to compare the methods for old samples. This is because a point estimate does not reflect well the difference between a symmetric Gaussian distribution and an asymmetric Poisson distribution, which here has a fast rise on the low concentration side and a longer tail to higher concentrations. Figure 21(b) presents the geometric means of the pdf given by each method at the point of the true values. For MB, Gaussian pdfs were assumed for the results, and results with near-zero uncertainties were not used. As can be seen, on average, CAR gives 30% higher probabilities for the true values.

Figure 22(a) shows the uncertainties from the methods for old samples. The average uncertainty of MB is below the counting statistical error, which is clearly unrealistic. The bias of MB towards too small uncertainties results from the fact that only the variance corresponding to the standard error of the mean is unbiased, leaving the important estimate itself as biased. This problem is independent of the age of the sample, and MB also suffers from this bias when applied to modern samples (see Figure 25 below). The uncertainty estimates from CAR are reliable and more stable (dark grey area) than the uncertainties given by MB (light grey area). The stability of the uncertainties will be further expounded below.

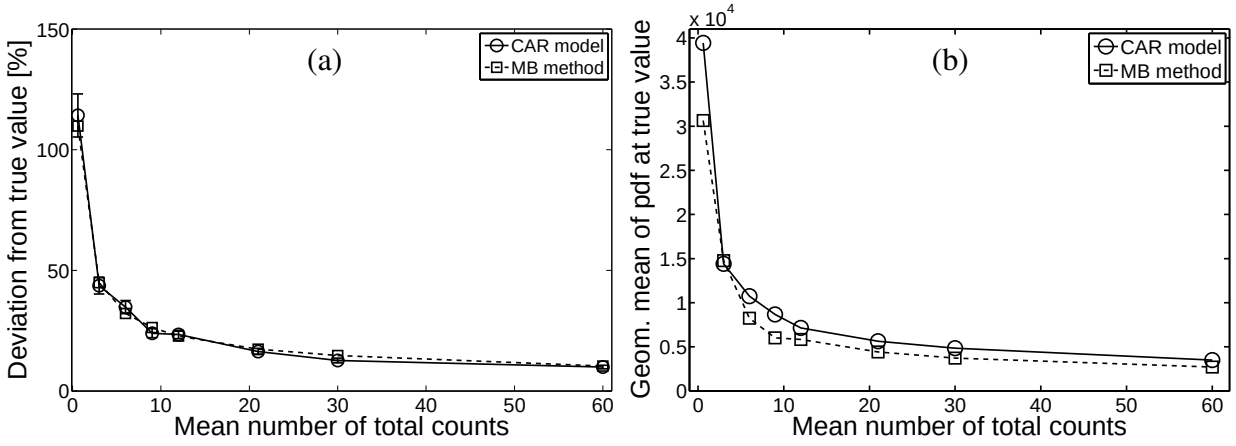

Figure 21: (a) The means of relative deviations between results with the CAR and MB methods and the known true values as a function of total counts from the sample. The mean number of counts in the simulated measurements were 0.1, 0.5, 1.0, 1.5, 2.0, 3.5, 5.0, or 10, with six measurements for each sample. (b) The geometric means of the pdf given by the method at the point of the true concentration.

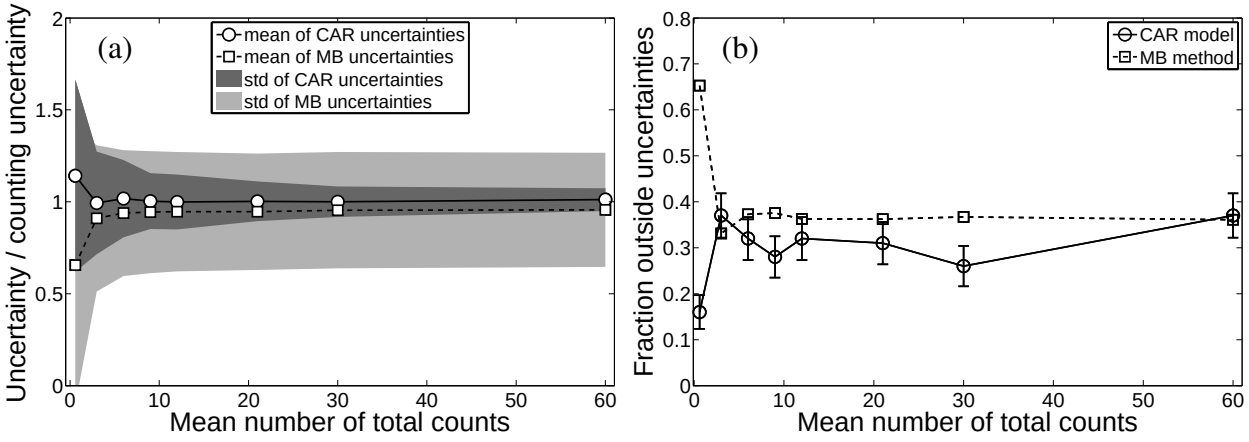

Figure 22: (a) Ratio of the uncertainty given by the method to the true mean counting statistical uncertainty as a function of the mean number of total counts. MB gives unrealistically low uncertainties. The random scatter in the uncertainties is much lower for CAR (dark grey area) than for MB (light grey area). The scatter was calculated as the sample standard deviation of the uncertainties. (b) Fraction of true values which are outside the uncertainties given by the methods.

Figure 22(b) shows for both methods the relative number of results that do not contain the true value. Because MB underestimates the errors, too many true values fall outside the quoted uncertainties. CAR hits the ideal 0.32 fraction for most points. For the very old samples, CAR uncertainties are a bit 'too safe'.

7.5 Scatter of uncertainties and number of measurements

The measured ratios are not the only information we have about an AMS run. In addition, we know that the ^{14}C counts are Poisson distributed. Hence, from the measured ^{14}C counts we know what scatter to expect from the underlying Poisson distribution and therefore what are the relevant uncertainties for the concentrations. By taking this simple information into account, one can significantly improve the quality of the results. However, because there are other sources of error in the measurements, the counting statistical uncertainty cannot be assumed to the final result directly. In effect, the whole CAR model is needed, to take the other sources of error into account adaptively and to propagate the uncertainty from the standard measurements to the final result. Note that the present problem of how to combine known information about the uncertainty with the sampling based estimates is an instance of a rather general problem, which in the AMS context has been clearly explained by Currie [82]. Up to this point the problem has remained unsolved, at least in the AMS case. To see the difference that the information about the counting statistics makes, simulations with zero trend were made. The number of measurements per sample varied from one to ten and the expected number of ^{14}C counts in one measurement was 18000.

Figure 23 shows the scatter of the results for both methods. Each point represents the uncertainty estimate and the deviation from the true concentration for one sample. Roughly 500 points were simulated with CAR and 5000 with MB for each plot. Because MB does not take the individual counting statistical uncertainties into account, there are both too small uncertainties, resulting in some true errors several times larger than the quoted uncertainties, and too large uncertainties, which undermine some of the information in the result. As expected, the CAR uncertainties have a very small scatter and are a bit larger than the counting statistical uncertainty of the measured sample, the difference coming mainly from the uncertainty in the standard measurements.

Figure 24 shows the accuracies, uncertainties, and the scatter for the uncertainties given by CAR and MB as a function of the number of measurements per sample.

Figure 25(a) shows the same quantities as Figure 24 for CAR and MBCSL, normalized to the counting statistical uncertainty. The fraction of points outside the quoted uncertainties for each method is shown in Figure 25(b). As can be seen, the uncertainties from the mean-based methods increasingly underestimate the true errors for smaller number of measurements. The average uncertainty of MBCSL is below the counting statistical uncertainty for cases where the uncertainty from the standard level is not significant. Again, CAR uncertainties have less scatter and are more reliable, with roughly the ideal 0.32 fraction of true values falling outside the quoted uncertainties.

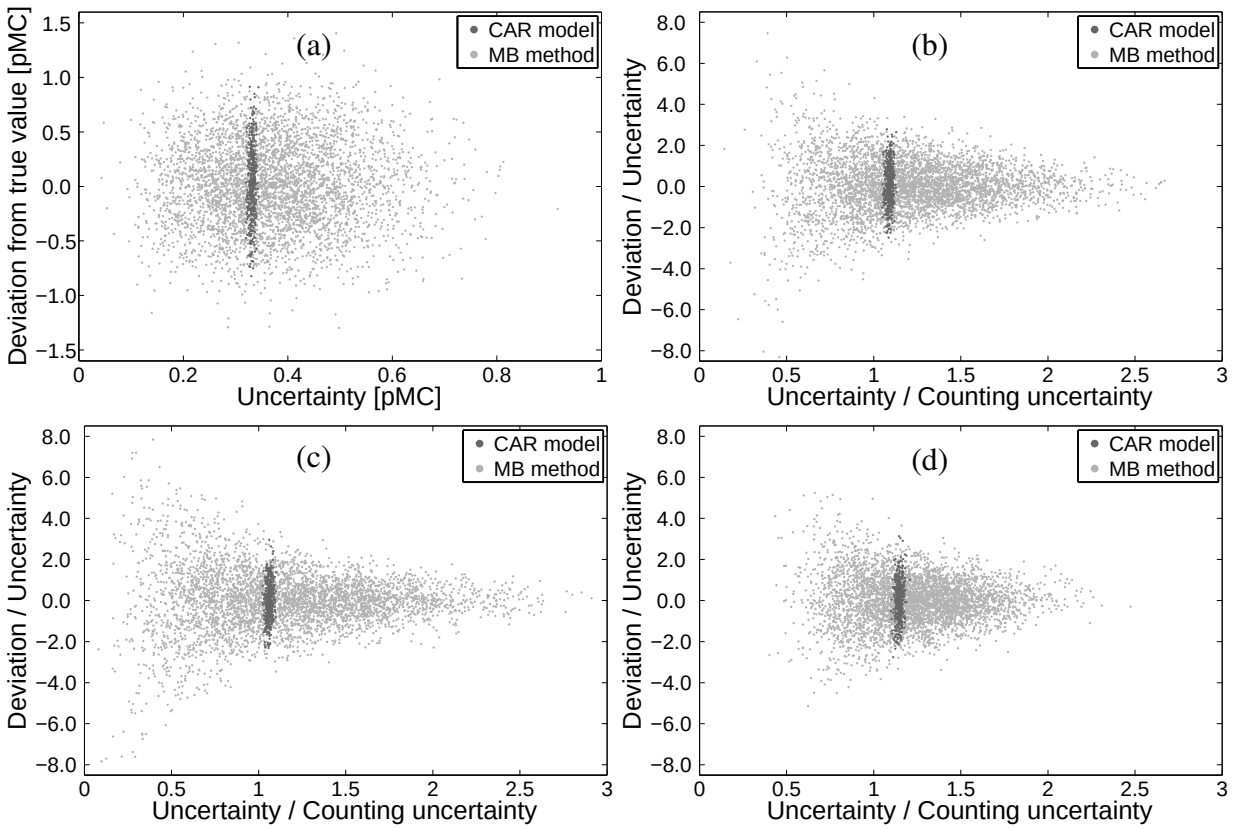

Figure 23: (a) A scatterplot of the uncertainty estimates (x-axis) and the true errors (y-axis) made by each method, six measurements per sample. (b) As for (a) but here the quoted uncertainty is normalized to the counting statistical uncertainty (x-axis), and the true error is normalized to the uncertainty estimate. (c) As for (b) but for four measurements per sample. (d) As for (b) but for ten measurements per sample.

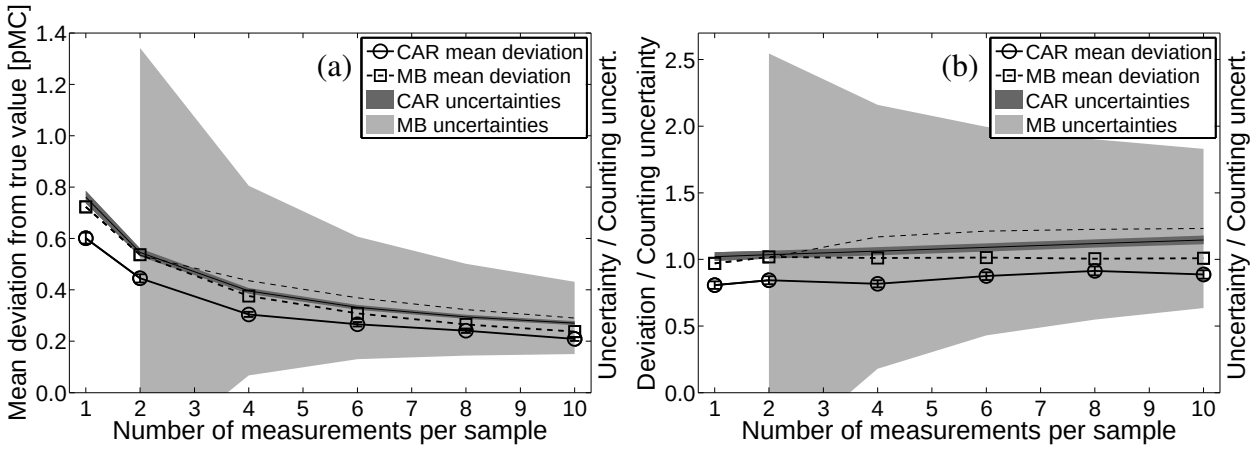

Figure 24: (a) Mean deviations from true concentration and the scatter of uncertainties for CAR and MB as a function of the number of measurements per sample. The uncertainties are represented by a line denoting the mean of the uncertainties and an area covering two standard deviations from the mean. (b) As for (a) but normalized to the counting statistical uncertainty.

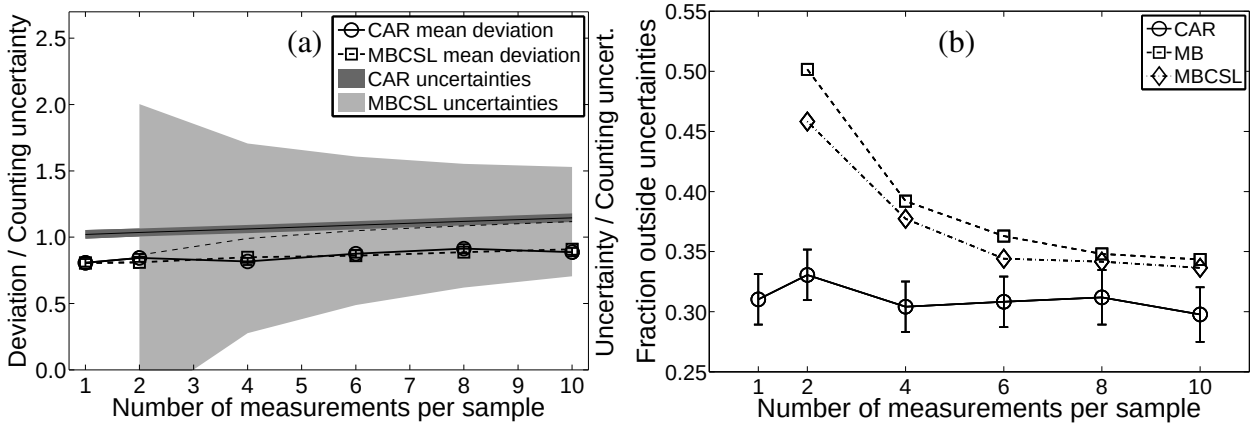

Figure 25: (a) As for Figure 24(b) but for CAR and MBCSL. (b) Fraction of the true concentration values which are outside the method's quoted uncertainties.

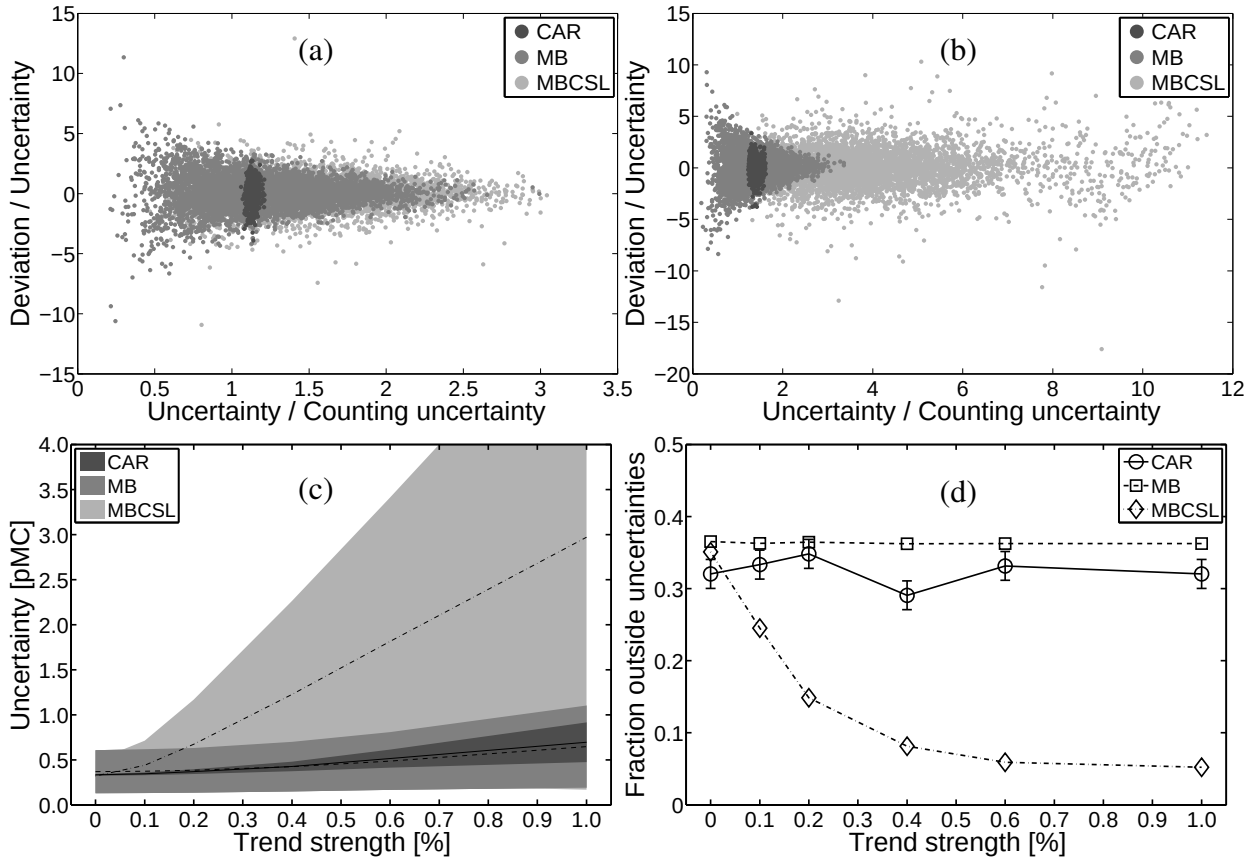

Figure 26: (a) Scatterplot of the uncertainties and true errors for each method for the case with 0.1% trend strength. (b) As for (a) but for 0.4% trend strength. (c) The mean and scatter of the uncertainties from each method as a function of trend strength. The areas cover two standard deviations. (d) The fraction of true concentration values falling outside the quoted uncertainties for each method.

Figure 26 shows the behaviour of the uncertainties as a function of trend strength (for the corresponding accuracies, see Figure 19). As the trend increases, MBCSL starts to overestimate the uncertainties. MBCSL also has some 'impossible' $> 5\sigma$ outliers even when the uncertainty of the outlier is above the counting statistical uncertainty. The scatter of the MB uncertainties is smaller than that of the MBCSL uncertainties for high drift cases owing to the normalization to nearby standards. Again, MB underestimates the uncertainties slightly, and too many points fall outside the 1σ interval. The uncertainties from CAR remain reliable, covering roughly the ideal 0.68 fraction of the true values for all trend strengths. The very small scatter of the uncertainties for the low-drift case increases with the drift. This is as expected because the simulated random-walk trend varies significantly even for simulations that have the same random-walk parameters.

The above results show that by taking the counting statistical uncertainty into account rigorously, the stability and reliability of the uncertainty estimates can be improved significantly.

8 CONCLUSIONS AND FUTURE RESEARCH

After much work, the Helsinki AMS system is now operational. The main parts of the system are documented in this thesis and the present performance is described. The present precision of the system is lower than that of the high-precision laboratories but is adequate for some applications. The background of the machine is comparable to that achieved in the best laboratories. Future modifications of the machine should include faster switching of the injector magnet field, which would result in improved precision. There is also room for improvement in the ion optics of the injector. Measurements of heavier isotopes will probably require utilization of the full mass resolution of the injector magnet. In that case the ion beam focus should be at the position of the slits after the magnet, at least in the bending direction. To achieve this without beam loss, additional space should be provided before the injector magnet, the ESA in the injector should be modified to a spherical analyser, and the einzel lens should be replaced with an electrostatic lens capable of focusing the horizontal and vertical directions independently.

The terminal voltage stabilization system could also be improved. In particular it would be interesting to see whether the GVM+CPU stabilization option could be improved sufficiently to stabilize the accelerator for AMS measurements.

Rare isotope detection is currently done with a silicon detector. The detector could be changed to a longer-lasting gas ionization detector with improved particle identification. A time of flight system could also be included to enable mass identification of the incoming ions. The particular type of detector depends, of course, on the isotope measured.

Some of the feasible applications for the Helsinki AMS are the measurements of ^{14}C in aerosols and iron artifacts, and biomedical studies where ^{14}C is used as a tracer. Pilot studies are in progress for the first two.

The CAR model of AMS data analysis presented in this thesis is a significant improvement over the previously used mean-based method. The CAR model for AMS data analysis has the following advantages:

- Uncertainties are stable.
- The method does not suffer from the slight bias to too small uncertainties that was observed for the mean-based methods.
- Rigorous control on the use of the standards is achieved. For a measurement with unstable throughput, only nearby standards are used. For a stable machine, all standard measurements can be used. This in turn results in better precision and accuracy for the concentration estimate.
- Gaussian pdfs are assumed only where appropriate.

- Reliable results are obtained even when there are correlations in the data (e.g. due to the use of the same standard values).
- Accurate and reliable analysis is provided for very old samples.
- Conversion to age is done using the full pdf of the concentration, thereby minimizing bias.
- Accurate and reliable analysis is possible even when there are only a few measurements.

Future research on the CAR model could take several directions. A faster computational algorithm or even an approximative algorithm for data analysis during the measurement would be an important practical improvement. More thorough theoretical and simulation studies of different priors could be done. Different laboratories could also use different priors for the CAR process parameters α and σ, typical to their own system. This would probably result in a slight further improvement in accuracy. Additional features like outlier detection and throughput correction with stored accelerator parameters could be included in the model. For AMS, the model should be applied to measurements of different isotopes. One interesting and almost minor modification would be the capability to take into account the memory effects from the previous measurements when using gas ion sources. Lastly, the main ideas of the model are clearly more general than the present application for AMS. Many measurements in physics and chemistry would benefit from the well-defined normalization to standards and from the rigorous way the model combines the known uncertainty in individual measurements with the observed sampling variance, resulting in stable uncertainties for the final results.

ACKNOWLEDGEMENTS

I am most grateful to Dr. Pertti Tikkanen for fruitful discussions, for the design of most parts of the AMS setup, and for introducing me to Bayesian theory. I wish to thank Professor Juhani Keinonen, head of the Department of Physical Sciences, for giving me the opportunity to work in the field of accelerator mass spectrometry and Bayesian statistical theory. My thanks are also due to the current and former heads of the Accelerator Laboratory, Professor Jyrki Räisänen and Dr. Eero Rauhala, for placing the facilities of the laboratory at my disposal, and to Dr. M. Oinonen and Professor H. Jungner, the current and former heads of the Dating Laboratory of the Finnish Museum of Natural History, for informative discussions.

Warmest thanks are expressed to my parents for supporting me all these years and to my wife Anu for her lovely presence during the past eight years.

Financial support from the Magnus Ehrnrooth Foundation and the Finnish Academy of Science and Letters, and a travel grant from the Helsinki University Chancellor are gratefully acknowledged.

Most importantly, I wish to thank God for the above people and for granting me entrance, also through this study, to a small part of His exquisite universe.

Helsinki, December 2007

V. P.

APPENDIX A SHORT DESCRIPTION OF ACCELERATOR IMPROVEMENTS

The upgrading of the Helsinki tandem accelerator began in 1998 with the design of an electrostatic deflector for the injector to enable the installation of two new ion sources to the injector. The deflector is rotatable and has 40° cylindrical electrodes that can also be raised above the beam line to let the beam from the old MISS ion source pass through the chamber. As well, an einzel lens fixed to the deflector chamber was designed and installed.

The MC-SNICS ion source for AMS was installed in 1999. Ion source supports were fixed to the injection magnet. Problems with Cs transfer from the Cs oven to the ionization area were remedied by installing heater for the tube between the Cs oven and the ion source. Stable > 10 μA $^{12}C^{-}$ currents were achieved.

A huge effort to convert hundreds of controls of the injector, accelerator, and beam line to computer control was commenced in 1996. Starting in 1997, controlling electronics were implemented with computers developed in the laboratory. The computers negotiate with a star-shaped optical CAN network via the CANKingdom protocol (by Kvaser). Later, a DeviceNet protocol using the present CAN network was developed, along with improved local computers. During 2006, it was decided that the automation implementation should be changed to a commercial system (CompactLogix from Allen-Bradley). Parts of the accelerator have been continuously taken into computer control and at present over 95% of the accelerator controls are in computer control. The operator interface to the controls is implemented with InTouch software (by Wonderware). Significant graphical design has been done for the roughly ten pages of controls for the different parts of the accelerator.

2000-2002

Terminal pumping with a 150 L/s turbo molecular pump was designed and installed. The pump runs at half of the nominal speed. As a means to decrease beam losses in the stripper, the old 4-mm-diameter stripper canal was enlarged to 10-mm diameter.

AMS measurements require reproducible throughput of the ions through the accelerator. Because of hysteresis, the magnetic fields of the bending magnets cannot be reproduced without a control loop utilizing the measurement of the field. For this reason, Hall probes for the measurement of the magnetic fields of the injector magnet and the switching magnet were installed and put under computer control. The analysing magnet was already equipped with an NMR probe for accurate measurement of the field.

To enable the off-axis measurement of isotopes, ^{13}C in particular, a new and enlarged vacuum chamber for the main analysing magnet was designed, constructed, and installed. Simultaneously, a chamber to enable off-axis beam measurements was designed and installed after the new analysing

magnet chamber. Mechanical feedthroughs with computer-controlled stepper-motors were installed in two positions of the off-axis chamber. An off-axis Faraday cup for current measurement and slits for terminal voltage stabilization were designed and fixed on the feedthroughs.

The switching magnet 60° beam line was rebuilt for AMS. Ion-optics calculations were done to optimize the throughput of ions to the detector and to minimize the effect of the terminal ripple on the beam throughput. While it was possible to optimize the achromaticity of the AMS beam line, total achromaticity was not achievable without changing the whole high energy beam line starting from the analysing magnet. A 30° high-energy electrostatic analyser was purchased from Danfysik for ion energy-filtering. Corresponding beam line supports and alignment equipment were designed and installed with the analyser. A 160 L/s ion pump was installed on the top of the analyser. The ion pump current enables fast monitoring of voltage sparks between the aluminium electrodes of the analyser. Better vacuum gauges, their connecting flanges, and beam profilometers were also installed for the AMS beam line. An additional 5 metres of beam line was constructed after the analyser. At the end of the beam line, a new vacuum chamber for pumping and another vacuum chamber for the detector were designed, constructed and installed, along with pumps and vacuum controls.

A small retractable Faraday cup was designed and installed in front of the detector. The Faraday cup geometry was optimized for electron suppression. The AMS detector is a semiconductor detector, attached to a flange at the end of the beam line. In addition, a small aluminium holder that supports a foil in front of the detector was designed.

With a large accelerator and long multi-component beam lines, it is essential to be able to monitor and adjust the ion paths easily and effectively. Seven profilometers (BPM80 from NEC) were bought and installed into the beam line. Profilometer and current gain selections were put under computer control.

To enable better beam tuning, the electrostatic quadrupole doublet that acted as a combined $x-y$ steerer and lens after the accelerator was updated. The earlier doublet, with independent pole voltages, was replaced with a separate steerer for correcting the beam position and a doublet with symmetric voltages of facing electrodes for focusing.

A new retractable Faraday cup and a limiting aperture for initial pilot beam tuning were designed and installed before the switching magnet.

The position of the ion exit and focusing properties of the switching magnet were changed by installing a 10° iron clamp at the exit point of the magnet for the AMS beam line. This enabled better focusing of the beam to the detector.

A database server (IndustrialSQL by Wonderware) was installed. The database stores all the relevant accelerator parameters from the automation network. Several interfaces, I/O servers, the database, and all the relevant tags in the database were configured.

2003

To decrease beam losses at the injector and accelerator, the beam line between the injector magnet and the accelerator was redesigned. A chamber with retractable Faraday cup and movable slits with larger maximum aperture was designed and installed to replace an old iris diaphragm. An electrostatic quadrupole triplet (NEC) was installed to replace an einzel lens. This was done to enable independent focusing in both directions. The lens was also installed closer to the accelerator to enable better matching of the emittance to the accelerator acceptance.

The operator interface is graphical and is implemented with a polling program (InTouch from Wonderware) with rather limited programming capabilities. A web-based application was developed, which queries raw data from the database, plots the values of relevant parameters, and calculates throughput profiles for different parameters. Similar capabilities were developed for use with MATLAB.

2004

A new charging belt for the accelerator was installed. The charging system was also changed from wire-grids in contact with the belt to non-contact charging needles in order to decrease mechanical wear of the belt surface. This has decreased the amount of dust in the accelerator tank.

A new terminal voltage stabilization system (NEC) was purchased and installed. In addition to the new system, a separate component that divides the slit signals with their sum was installed in the signal route before the stabilization system. This was done to make the stabilization signal independent of the beam current.

During ^{14}C measurements the terminal voltage is stabilized with slits and the CPU. It was soon realized that the molecular currents coming from highly pure carbon samples were very small. In order to enable stabilization with down to 10 pA currents, additional slit preamplifiers were designed and built.

2005

The terminal-facing parts of the GVM were observed to be oxidized and were cleaned and gold-plated. Bearings of the GVM were replaced.

Switching between the measured isotopes is done by varying the magnetic field of the injector magnet. A CAN box for the injector magnet Hall probe readout was installed. Another computer was installed for the control of the magnet current. A PID algorithm was programmed to the accelerator control software. The changes decreased the injector field switching time from about 60 seconds to about 30 seconds.

A 1600-L/s turbo pump was installed to the injector at the entrance of the accelerator because the beam throughput is sensitive to vacuum in the low-energy tubes, and measurement had shown the throughput to be sensitive to the gas pressure in the stripper. A smaller 250-L/s turbo pump was installed after the accelerator, and, a 600-L/s ion pump at the end of the pumping tube was replaced with a 500-L/s turbo pump to enable pumping of argon gas.

A new sample press was designed and constructed in 2005. The old sample press could not deliver constant distance of the sample material from the cathode surface, and some carbon spread over the cathode front surface. This resulted in different emittances for the samples. The new press gives a constant 0.5 mm distance of the carbon from the cathode surface. In addition to more reproducible emittances, the parts of the press that are in contact with the sample material during the pressing are exchangeable and easy to clean, minimizing sample contamination.

The high energy ESA was observed to spark and cause damage to nearby control units. Relevant control units were made more spark-proof, and electric shielding was increased.

During a ^{13}C measurement the same ^{13}C ion current is used to stabilize the terminal voltage. Separate slits therefore interfered with the measurement of ^{13}C current. A new Faraday cup was designed and installed to the off-axis chamber with electron suppression and slits inside the cup. The necessary low-noise and low-leak electronics were designed. The setup enables both slit stabilization and readout of the total beam current.

Computer control of the AMS measurement was optimized, resulting in shorter isotope switching times and a more error-free operation.

A smaller 8-mm-diameter stripper canal and smaller 12-mm-diameter shunts were installed.

2006

The charging belt of the accelerator had to be replaced twice. Non-contact charging system was tested and then replaced with a charging system with steel wire brushes in contact with the belt. An optical fibre was drawn to the terminal enabling transfer of data from a CompactRIO (National Instruments) processor inside the terminal. Several parameters in the terminal (e.g., recharging voltages and currents) can now be monitored. Stripper pressure leaks were protected from outside fluctuations of gas flow and temperature with a special chamber, removing the oscillation in the stripper pressure. A new high voltage cascade for recharging was installed in the terminal. In the injector, an old preaccelerating voltage source was found to be unstable and was replaced with a new one. This significantly improved beam quality for all three ion sources using the voltage source.

To ease the high-voltage conditioning of the ESA, the DeviceNet unit controlling it was replaced by a CompactRIO processor, which proved to be more spark-proof. Software was made to automatically condition the ESA by applying appropriate voltage ramps.

The slits before the analysing magnet were fixed to the magnet to enable constant energy calibration and reproducible slit positions between the measurements.

A decision was made to move to a new automation system. The system (CompactLogix and POINT I/O systems from Allen-Bradley) uses ethernet technology between a centralized controller and the various I/O points in the field.

2007

The parameters that control the terminal voltage system were taken under the new Allen-Bradley automation system. A CompactRIO computer was installed in the accelerator terminal to monitor the charging system and stripper gas leaks.

APPENDIX B SHORT INTRODUCTION TO BAYESIAN INFERENCE

The Bayesian view of probability is that a probability is a state of belief, always conditional on some background information I. Only in some cases should probabilities be thought of as frequencies.

At the heart of Bayesian methods is the Bayes' theorem, which follows directly from the basic identities of probability theory. The probability that both A and B are true given that background information I is true, is, using the product rule of probability,

$$p(\mathrm{A},\mathrm{B}|\mathrm{I}) = p(\mathrm{A}|\mathrm{I})p(\mathrm{B}|\mathrm{A},\mathrm{I}) = p(\mathrm{B}|\mathrm{I})p(\mathrm{A}|\mathrm{B},\mathrm{I}). \tag{42}$$

This can be rewritten in the form

$$p(\mathrm{B}|\mathrm{A},\mathrm{I}) = \frac{p(\mathrm{B}|\mathrm{I})p(\mathrm{A}|\mathrm{B},\mathrm{I})}{p(\mathrm{A}|\mathrm{I})}. \tag{43}$$

Equation (43) is the Bayes' theorem, which is a formula for updating the probability for B, when we have additional information A. This kind of inversion problem is very common in science. For example, after measuring data $\mathbf{Y}$, the probability of parameters $\mathbf{P}$ in theory M can be calculated, rewriting Eq. (43) as

$$p(\mathbf{P}|\mathbf{Y},\mathrm{M}) = \frac{p(\mathbf{P}|\mathrm{M})\ p(\mathbf{Y}|\mathbf{P},\mathrm{M})}{p(\mathbf{Y}|\mathrm{M})}, \tag{44}$$

where $p(\mathbf{P}|\mathrm{M})$ is a prior probability distribution for the parameters, $p(\mathbf{Y}|\mathbf{P},\mathrm{M})$ is the likelihood, and $p(\mathbf{Y}|\mathrm{M})$ is the marginal distribution. Note that the likelihood is not a probability distribution with respect to the parameters $\mathbf{P}$ and hence inferences based solely on the likelihood are not encouraged. Because the marginal distribution is an integral of the numerator over all parameter values (marginalization over the parameters), $p(\mathbf{Y}|\mathrm{M}) = \int p(\mathbf{P}|\mathrm{M})\ p(\mathbf{Y}|\mathbf{P},\mathrm{M})\ \mathrm{d}\mathbf{P}$, it is essentially a normalization constant in the equation. The Bayes' theorem can also be used to compare different theories by replacing $\mathbf{P}$ by some discrete model indicator and M by information common to the theories.

The Bayes' theorem is a highly useful tool, also applicable in situations where frequentist statistics cannot be used or give erroneous results. Some problems exist nevertheless. Prior selection is often difficult and not without ambiguity. Moreover, since the theorem can only compare hypotheses, a single hypothesis cannot be rejected.

It is often claimed that Bayesian model selection incorporates Occam's razor, but this is the case only as far as more complex models make broader predictions. So, not surprisingly, Bayesian model selection selects models on the basis of prior expectations for the data, i.e. model predictions.

References

[1] C. Tuniz, J. Bird, D. Fink, and G. F. Herzog, *Accelerator mass spectrometry: ultrasensitive analysis for global science* (CRC Press, Boca Raton, 1998).

[2] L. W. Alvarez and R. Cornog, ^{3}*He in helium*, Phys. Rev. **56**, 287 (1939).

[3] R. A. Muller, *Radioisotope dating with a cyclotron*, Science **196**, 489 (1977).

[4] F. L. Bennett, W. E. Sondheim, R. P. Beukens, M. R. Clover, H. E. Gore, R. B. Liebert, A. E. Litherland, and K. H. Purser, *Radiocarbon dating using electrostatic accelerators: negative ions provide the key*, Science **198**, 508 (1977).

[5] D. E. Nelson, R. G. Korteling, and W. R. Stott, *Carbon-14: direct detection at natural concentrations*, Science **198**, 507 (1977).

[6] G. M. Raisbeck, F. Yiou, M. Fruneau, and J. M. Loiseaux, *Beryllium-10 mass spectrometry with a cyclotron*, Science **202**, 217 (1978).

[7] G. M. Raisbeck, F. Yiou, and C. Stephan, ^{26}*Al with a cyclotron*, J. de Physique Lett. **40L**, 241 (1979).

[8] D. Elmore, D. Fulton, M. R. Clover, J. R. Marsden, J. R. Gove, H. Naylor, H. Purser, L. R. Kilius, R. P. Beukens, and A. E. Litherland, *Analysis of* ^{36}*Cl in environmental water samples using an electrostatic accelerator*, Nature **277**, 22 (1979).

[9] G. M. Raisbeck, F. Yiou, A. Peghaire, J. Guillot, and J. Uzureau, *Instability of* KH_3^1 *and potential implications for detection of* ^{41}*Ca with a tandem electrostatic accelerator*, Proc. Symp on Accelerator Mass Spectrometry, Argonne National Laboratory, ANL/PHY-81-1 426 (1981).

[10] D. Elmore, H. E. Gove, R. Ferraro, L. Kilius, H. W. Lee, K. H. Chang, R. P. Beukens, A. E. Litherland, C. J. Russo, K. H. Purser, M. T. Murrell, and R. C. Finkel, *Determination of* ^{129}*I using tandem accelerator mass spetrometry*, Nature **286**, 138 (1980).

[11] *Proceeding of the First Conference on Radiocarbon Dating with Accelerators*, edited by H. E. Gove (University of Rochester, New York, 1978).

[12] A. E. Litherland, *Ultrasensitive mass spectrometry with accelerators*, Ann. Rev. of Nucl. and Part. Sci. **30**, 437 (1980).

[13] *Proceedings of the 2nd Int. Symp. on Accelerator Mass Spectrometry*, edited by W. Henning, W. Kutschera, R. K. Smither, and J. L. Yntema (ANL/PHY-81-1, Argonne National Laboratory, Chicago, 1981), Vol. 1L.

[14] W. Wölfli, H. A. Polach, and H. H. Andersen, *Proceedings of the 3rd Int. Symp. on Accelerator Mass Spectrometry*, Nucl. Instrum. Methods Phys. Res. B **29**, (1984).

[15] W. Broecker, A. Mix, M. Andree, and H. Oechger, *Radiocarbon measurements on coexisting benthic and planktic foraminifera shells: potential for reconstructing ocean ventilation times over the past 20000 years*, Nucl. Instrum. and Meth. B **233**, 311 (1984).

[16] D. Elmore and F. M. Phillips, *Accelerator mass spectrometry for measurement of long-lived radioisotopes*, Science **236**, 543 (1987).

[17] H. E. Gove, A. E. Litherland, and D. Elmore, *Proceedings of the 4th Int. Symp. on Accelerator Mass Spectrometry*, Nucl. Instrum. Methods Phys. Res. B **29**, (1987).

[18] W. Kutschera, *Accelerator mass spectrometry: a versatile tool for research*, Nucl. Instrum. and Meth. B **50**, 252 (1990).

[19] M. Suter, *Accelerator mass spectrometry: state of the art in 1990*, Nucl. Instrum. and Meth. B **52**, 211 (1990).

[20] F. Yiou and G. M. Raisbeck, *Proceedings of the 5th Int. Conf. on Accelerator Mass Spectrometry*, Nucl. Instrum. Methods Phys. Res. B **52**, (1990).

[21] R. C. Finkel and M. Suter, *AMS in the earth sciences: technique and applications*, Advances in Analytical Geochemistry **1**, 1 (1993).

[22] M. Paul, *New developments and challenges in accelerator mass spectrometry*, Nucl. Instrum. and Meth. A **328**, 330 (1993).

[23] L. K. Fifield, D. Fink, and C. Tuniz, *Proceedings of the 6th Int. Conf. on Accelerator Mass Spectrometry*, Nucl. Instrum. Methods Phys. Res. B **92**, (1994).

[24] A. J. T. Jull, J. W. Beck, and G. S. Burr, *Proceedings of the 7th Int. Conf. on Accelerator Mass Spectrometry*, Nucl. Instrum. Methods Phys. Res. B **123**, (1997).

[25] W. Kutschera, G. Golser, A. Priller, and B. Strohmaier, *Proceedings of the 8th Int. Conf. on Accelerator Mass Spectrometry*, Nucl. Instrum. Methods Phys. Res. B **172**, (1999).

[26] M. Suter, *25 years of AMS - a review of recent developments*, Nucl. Instrum. Methods Phys. Res. B **223-224**, 139 (2004).

[27] S. Jiang, A. Yu, Y. Cui, Z. Zhou, D. Luo, and Q. Li, *Determination of tritium using a small Van de Graaff accelerator*, Nucl. Instrum. Methods Phys. Res. B **5**, 226 (1984).

[28] S. E. King, G. W. Phillips, R. A. August, L. A. Beach, J. H. Cutchin, and C. Castaneda, *Detection of tritium using accelerator mass spectrometry*, Nucl. Instrum. Methods Phys. Res. B **29**, 14 (1987).

[29] S. Jiang, Y. Liu, Y. Cui, and W. Xun, *Determination of ^{3}He with a tandetron accelerator at 0.8 MV*, Nucl. Instrum. Methods Phys. Res. B **29**, 226 (1987).

[30] G. M. Raisbeck and F. Yiou, *Measurement of ^{7}Be by accelerator mass spectrometry*, Earth Planet. Sci. Lett. **89**, 103 (1988).

[31] G. M. Raisbeck, F. Yiou, D. Bourles, J. Lestringuez, and D. Deboffle, *Measurements of ^{10}Be and ^{26}Al with a Tandetron AMS facility*, Nucl. Instrum. Methods Phys. Res. B **29**, 22 (1987).

[32] J. Klein and R. Middleton, *Accelerator mass spectrometry and the University of Pennsylvania*, Nucl. Instrum. Methods Phys. Res. B **5**, 129 (1984).

[33] M. Suter, R. Balzer, G. Bonani, H. Hofmann, E. Morenzoni, M. Nessi, W. Wölfli, M. Andree, J. Beer, and H. Oeschger, *Precision measurements of ^{14}C in AMS – some results and prospects*, Nucl. Instrum. Methods Phys. Res. B **5**, 117 (1984).

[34] M. S. Thomsen, J. Heinemeier, P. Hornshoj, and N. Rud, *Isotopic ratio of ^{22,24}Na measured by accelerator spectrometry*, Nucl. Instrum. Methods Phys. Res. B **28**, 433 (1987).

[35] R. Middleton and J. Klein, *^{26}Al measurements and applications*, Phil Trans Roy. Soc. A **323**, 121 (1987).

[36] D. Elmore, N. Anantaraman, H. W. Fulbright, H. E. Gove, H. S. Hans, K. Nishiizumi, M. T. Murell, and M. Honda, *Half-life of ^{32}Si from tandem accelerator mass spectrometry*, Phys. Rev. Lett. **1980**, 589 (45).

[37] W. Kutschera, W. Henning, M. Paul, R. Smither, E. J. Stephenson, J. L. Yntema, E. E. Alburger, J. B. Cumming, and G. Harbottle, *Measurement of the ^{32}Si half-life via tandem accelerator mass spectrometry*, Phys. Rev. Lett. **1980**, 592 (45).

[38] L. K. Fifield, T. R. Ophel, J. R. Bird, and R. F. Davie, *The chlorine-36 measurement program at the Australian National University*, Nucl. Instrum. Methods Phys. Res. B **29**, 114 (1987).

[39] D. Elmore, J. J. Conard, P. W. Kubik, H. E. Gove, M. Wahlen, J. Beer, and M. Suter, *^{36}Cl and ^{10}Be profiles in Greenland ice: dating and production rate variations*, Nucl. Instrum. Methods Phys. Res. B **29**, 207 (1987).

[40] D. Fink, R. Middleton, J. Klein, and P. Sharma, *^{41}Ca: measurement by accelerator mass spectrometry and applications*, Nucl. Instrum. Methods Phys. Res. B **47**, 79 (1990).

[41] G. Korschinek, H. Morinaga, E. Nolte, E. Preisenberger, U. Ratzinger, A. Urban, P. Dragovitsch, and S. Vogt, *Accelerator mass spectrometry with completely stripped ^{41}Ca and ^{53}Mn ions at the Munich tandem laboratory*, Nucl. Instrum. Methods Phys. Res. B **52**, 498 (1987).

[42] G. Korschinek, D. Muller, t. Faestermann, A. Gillitzer, E. Nolte, and M. Paul, *Trace analysis of ^{55}Fe in biosphere and technology by means of AMS*, Nucl. Instrum. Methods Phys. Res. B **52**, 498 (1990).

[43] M. Paul, L. K. Fifield, D. Fink, A. Albrecht, G. L. Allan, G. Herzog, and C. Tuniz, *Measurements of ^{59}Ni in meteorites by accelerator mass spectrometry*, Nucl. Instrum. Methods Phys. Res. B **83**, 275 (1993).

[44] W. Kutschera, *Rare particles*, Nucl. Instrum. Methods Phys. Res. B **5**, 420 (1984).

[45] D. L. Knies, K. S. Grabowski, D. J. Treacy, T. M. DeTruck, and H. A. Enge, in *Status of the Naval Research Laboratory trace element accelerator mass spectrometer: characterization of the Pretzel magnet*, edited by J. L. Duggan and I. L. Morgan (AIP Press, New York, 1997), p. 783.

[46] S. Jiang, J. Guo, S. Jiang, C. Li, A. Cui, M. He, S. Wu, and S. Li, *Determination of the half-life of* ^{79}*Se with the accelerator mass spectrometry technique*, Radiocarbon **38**, 56 (1996).

[47] M. Paul, D. Berkovits, L. D. Cecil, H. Feldstein, A. Hershkowitz, P. R. Livens, and S. Vogt, *Environmental* ^{90}*Sr measurements*, Nucl. Instrum. Methods Phys. Res. B **123**, 394 (1997).

[48] G. Korschinek, T. Faestermann, S. Kastel, K. Knie, H. J. Maier, J. Fernandez-Niello, M. Rothenberger, and L. Zerle, *AMS for* $M > 36$ *with a gas-filled magnetic spectrograph*, Nucl. Instrum. Methods Phys. Res. B **92**, 146 (1994).

[49] L. R. Kilius, J. C. Rucklidge, and A. E. Litherland, *Accelerator mass spectrometry of* ^{129}*I at IsoTrace*, Nucl. Instrum. Methods Phys. Res. B **20**, 72 (1987).

[50] M. Paul, D. Fink, G. Hollos, A. Kaufmann, W. Kutschera, and M. Magaritz, *Measurement of* ^{129}*I concentration in the environment after the Chernobyl reactor acccident*, Nucl. Instrum. Methods Phys. Res. B **29**, 341 (1987).

[51] P. Gartenmann, R. Golser, P. Haas, W. Kutschera, M. Suter, H. A. Synal, M. J. M. Wagner, and E. Wild, *Absolute measurement of* ^{126}*Sn radionuclide concentration with AMS*, Nucl. Instrum. Methods Phys. Res. B **114**, 125 (1996).

[52] L. R. Kilius, M. A. Grawan, A. E. Litherland, M. J. Nadeau, J. C. Rucklidge, and X.-L. Zhao, *Heavy element analysis by low energy accelerator mass spectrometry*, Nucl. Instrum. Methods Phys. Res. B **40/41**, 745 (1989).

[53] H. Ernst, G. Korschinek, P. Kubik, W. Mayer, H. Morinaga, E. Nolte, W. henning, W. Kutschera, M. Muller, and D. Schull, ^{205}*Pb: accelerator mass spectrometry of a very heavy radioisotope and the solar neutrino problem*, Nucl. Instrum. Methods Phys. Res. B **5**, 426 (1984).

[54] X.-L. Zhao, M.-J. Nadeau, L. R. Kilius, and A. E. Litherland, *The first detection of naturally occurring* ^{238}*U with accelerator mass spectrometry*, Nucl. Instrum. Methods Phys. Res. B **92**, 249 (1994).

[55] L. K. Fifield, A. P. Clacher, K. Morris, S. J. King, R. G. Cresswell, J. P. Day, and F. R. Livens, *AMS of the planetary elements*, Nucl. Instrum. Methods Phys. Res. B **123**, 400 (1997).

[56] A. S. Ivanov, G. F. Kirshin, V. M. Latmanizov, A. V. Lysov, V. Mikhailov, G. Roshal', and S. Subbotkin, *EGP-10 type charge-changing electrostatic accelerator*, Atomnaya Energiya **34**, 401 (1973), English translation: Soviet Atomic Energy 34 (5) (1973) 493–49.

[57] B. M. Hochberg, V. D. Mikhailov, and V. A. Romanov, *Some tandem accelerators in the Soviet Union*, Nucl. Instrum. Meth. **122**, 119 (1974).

[58] H. J. Hofmann, G. Bonani, M. Suter, and W. Wölfli, *Charge state distributions and isotopic fractionation*, Nucl. Instrum. and Meth. B **29**, 100 (1987).

[59] U. Rohrer, PSI Graphic Transport based on a CERN-SLAC-FERMILAB version by K.L. Brown et al.

[60] National Electrostatic Corporation, personal communication.

[61] D. Dahl, 2000, simion 3D version 7.0 manual.

[62] D. C. Carey, *The optics of charged particle beams* (Harwood Academic Publishers, Chur, 1987).

[63] T. Joy, *Simulation of heavy ion scattering at strippers in beam optics calculations for tandem van de graaff accelerators*, Nucl. Instrum. and Meth. **106**, 237 (1973).

[64] M. Friedrich, *Ionenoptische untersuchungen am Rossendorfer tandembeschleuniger EGP-10-1* (Akademie der Wissenschaften der DDR, Dresden, Germany, 1986), Vol. ZfK-593.

[65] M. Berz, *Computational aspects of optics design and simulation: COSY INFINITY*, Nucl. Instrum. and Meth. A **298**, 473 (1990).

[66] M. Berz, *Modern map methods in particle beam physics* (Academic Press, San Diego, 1999).

[67] A. A. Geraci, T. A. Barlow, M. Portillo, J. A. Nolen, K. W. Shepard, K. Makinno, and M. Berz, *High-order maps with acceleration for optimization of electrostatic and radio-frequency ion-optical elements*, Rev. Sci. Instrum. **73**, 3174 (2002).

[68] D. Elmore, N. Conard, P. W. Kubik, and J. Fabryka-Martin, *Computer controlled isotope ratio measurements and data analysis*, Nucl. Instrum. Methods Phys. Res. B **5**, 233 (1984).

[69] M. Stuiver, *Reporting of ^{14}C data*, Radiocarbon **19**, 355 (1977).

[70] D. J. Donahue, T. W. Linick, and A. J. T. Jull, *Isotope-ratio and backround corrections for accelerator mass spectrometry radiocarbon measurement*, Radiocarbon **32**, 135 (1990).

[71] R. E. Taylor and J. Southon, *Use of natural diamonds to monitor ^{14}C AMS instrument background*, Nucl. Instrum. Methods Phys. Res. B **259**, 282 (2007).

[72] C. Bronk Ramsey, *Development of the radiocarbon calibration program OxCal*, Radiocarbon **43**, 355 (2001).

[73] J. A. Christen and G. Nicholls, *Random-walk radiocarbon calibration*, Mathematics Department, University of Auckland, Technical Report **#457**, (2000).

[74] C. E. Buck, D. G. P. Aguilar, C. D. Litton, and A. O'Hagan, *Bayesian nonparametric estimation of the radiocarbon calibration curve*, Bayesian Analysis **1**, 265 (2005).

[75] C. Bronk Ramsey, *Radiocarbon calibration and analysis of stratigraphy: the OxCal program*, Radiocarbon **37**, 425 (1995).

[76] J. A. Christen, R. S. Clumo, and C. D. Litton, *A Bayesian approach to the use of ^{14}C dates in the estimation of the age of peat*, Radiocarbon **37**, 431 (1995).

[77] J. A. Christen, *Bayesian interpretation of radiocarbon results* (PhD thesis, University of Nottingham, Nottingham, 1994).

[78] V. Palonen and P. Tikkanen, *Spectral analysis of the IntCal98 calibration curve: a Bayesian view*, Nucl. Instrum. Meth. Phys. Res. **B 223-224**, 359 (2004).

[79] V. Palonen and P. Tikkanen, *Bayesian periodic signal detection applied to IntCal98 data*, Radiocarbon **46**, 979 (2004).

[80] V. Palonen, *Bayesian method for frequency detection in paleoclimatic proxy data*, MaxEnt04 Conference Proceedings, AIP Conference Proceedings **735**, 252 (2004).

[81] V. Palonen and P. Tikkanen, *Bayesian spectral analysis of raw tree-ring IntCal04 data: No continuous sinusoids – some short duration sinusoids*, Nucl. Instrum. Methods Phys. Res. B **259**, 426 (2007).

[82] L. A. Currie, *Optimal estimation of uncertainty intervals for accelerator and decay counting*, Nucl. Instrum. Methods Phys. Res. B **92**, 188 (1994).

[83] D. J. Donahue, A. J. T. Jull, T. W. Linich, A. Hatheway, L. J. Toolin, B. Gore, and P. E. Damon, *Some results from the Arizona TAMS facility: AMS ages of athletic, artistic, and animal artifacts*, Nucl. Instrum. Methods Phys. Res. B **29**, 169 (1987).

[84] G. S. Burr, D. J. Donahue, Y. Tang, J. W. Beck, L. McHargue, D. Diddulph, R. Cruz, and A. J. T. Jull, *Error analysis at the NSF-Arizona AMS facility*, Nucl. Instrum. Methods Phys. Res. B **259**, 149 (2007).

[85] F. H. Séguin, R. J. Schneider, G. A. Jones, and K. F. von Reden, *Optimized data analysis for AMS radiocarbon dating*, Nuclear Instruments and Methods in Physics Research B **92**, 176 (1994).

[86] R. H. Jones, *Longitudinal data with serial correlations: a state-space approach* (Chapman & Hall, London, 1993).

[87] L. D. Broemeling and P. Cook, *A Bayesian analysis of regression models with continuous errors with application to longitudinal studies*, Statistics in medicine **16**, 321 (1997).

[88] F. V. Jensen, *An introduction to Bayesian networks* (UCL Press, Gower Street, London, 1996).

[89] R. E. Kass and L. Wasserman, *Formal rules for selecting prior distributions: a review and annotated bibliography*, Carnegie Mellon University, PA, Technical Report **#583**, (1994).

[90] H. Jeffreys, *Theory of probability, 3rd ed.* (Oxford University Press, New York, 1939).

[91] A. Zellner, *An introduction to Bayesian inference in econometrics* (John Wiley & Sons, New York, 1971).

[92] A. Gelman, J. B. Carlin, H. S. Stern, and D. B. Rubin, *Bayesian data analysis, second edition* (Chapman & Hall/CRC, Boca Raton, 2003).

[93] W. R. Gilks, S. Richardson, and D. J. Spiegelhalter (eds), *Markov chain Monte Carlo in practice* (Chapman & Hall/CRC, Boca Raton, 1996).

[94] D. B. R. A. Gelman, *Inference from iterative simulation using multiple sequences*, Statistical Science **7**, 473 (1992).

[95] S. P. Brooks and A. Gelman, *General methods for monitoring convergence of iterative simulations*, Journal of Computational and Graphical Statistics **7**, 434 (1998).

[96] S. Särkkä and A. Vehtari, MCMC diagnostics toolbox for Matlab, Helsinki University of Technology (1999) http://www.lce.hut.fi/research/mm/mcmcdiag/.

[97] B. J. Smith, Bayesian output analysis program (BOA), Version 1.1.5, University of Iowa (2005) http://www.public-health.uiowa.edu/boa.

[98] E. T. Jaynes, *Probability theory: the logic of science* (Cambridge University Press, Cambridge, 2003).